Construction of protein oligomers with heme-coordinating methionine depleted *c*-type cytochrome mutant and resonance Raman studies on oxygenated *c*-type cytochromes

---

ヘム配位メチオニン欠損 *c* 型シトクロム変異体を用いたタンパク質多量体の作製と酸素化型 *c* 型シトクロムの共鳴ラマン研究

ACADEMIC DISSERTATION

MOHAN ZHANG

2017 September

Graduate School of Materials Science

Nara Institute of Science and Technology

Supramolecular Science

Contents

List of Abbreviation

Cyt *c*	:	Cytochrome *c*
Cyt cb_{562}	:	Cytochrome cb_{562}
Cyt c_{551}	:	Cytochrome c_{551}
Cyt c_{552}	:	Cytochrome c_{552}
RNase A	:	Ribonuclease A
Mb	:	Myoglobin
Hb	:	Hemoglobin
HT	:	*Hydrogenobacter thermophilus*
PA	:	*Psuedomonas aeruginosa*
His	:	Histidine
Asp	:	Aspartic acid
Pro	:	Proline
Ala	:	Alanine
Lys	:	Lysine
Gly	:	Glycine
Cys	:	Cysteine
Met	:	Methionine

Tyr	:	Tyrosine
Phe	:	Phenylalanine
Ile	:	Isoleucine
RMSD	:	Root-mean-square deviation
FPLC	:	Fast protein liquid chromatography
SEC	:	Size exclusion chromatography
CD	:	Circular dichroism

Chapter 1

General introduction

1-1 Protein design

Protein design has become a useful method to create novel artificial proteins and has been applied to biotechnology and pharmaceutics, such as bio-sensors and bio-imaging. Protein supramolecules, including protein complexes, are attractive because they can provide more sophisticated structures and functions than those of monomeric proteins. Although it is difficult to control protein–protein interactions, such as hydrophobic packing, electrostatic interaction, hydrogen bonding (H-bond), and van der Waals interaction, many kinds of protein–protein interactions have been used to control the protein supramolecular formation (*1-4*).

Protein–protein interactions have been controlled by introduction of metal-binding sites into the protein surface (Figure 1.1). Artificial protein structures have been constructed by introduction of metal binding sites into an α-helix bundle protein (*5*), but undesirable structures may also form in addition to the desired structure.

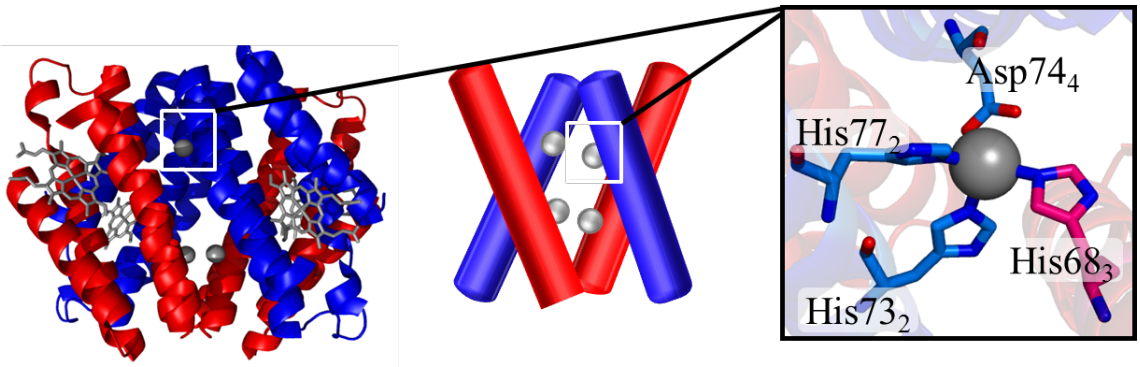

Figure 1.1 Crystal structure of the 4 Zn / 4 His$_4$-cyt *cb*$_{562}$ assembly (PDB: 2QLA). The hemes are shown as stick models. Zn-coordinating aspartic acid and histidines are shown as stick models. The Zn ions are shown as gray spheres.

Attempts to create hemeprotein oligomers have been performed. Hemeproteins such as cytochrome (cyt) *c* and horseradish peroxidase have been chosen as a protein scaffold to construct supramolecular hemoproteins by chemical methods, attaching a heme at the protein surface (*6-9*). Cyt *cb*$_{562}$ and myoglobin mutants have also been used to construct protein polymers by successive intermolecular heme−heme pocket interactions. Formations of an one-dimensional linear structure, a two-dimensional network, and a three-dimensional cluster were controlled by changing the molar ratio of the hemeprotein and pivot molecule (Figure 1.2) (*10-12*).

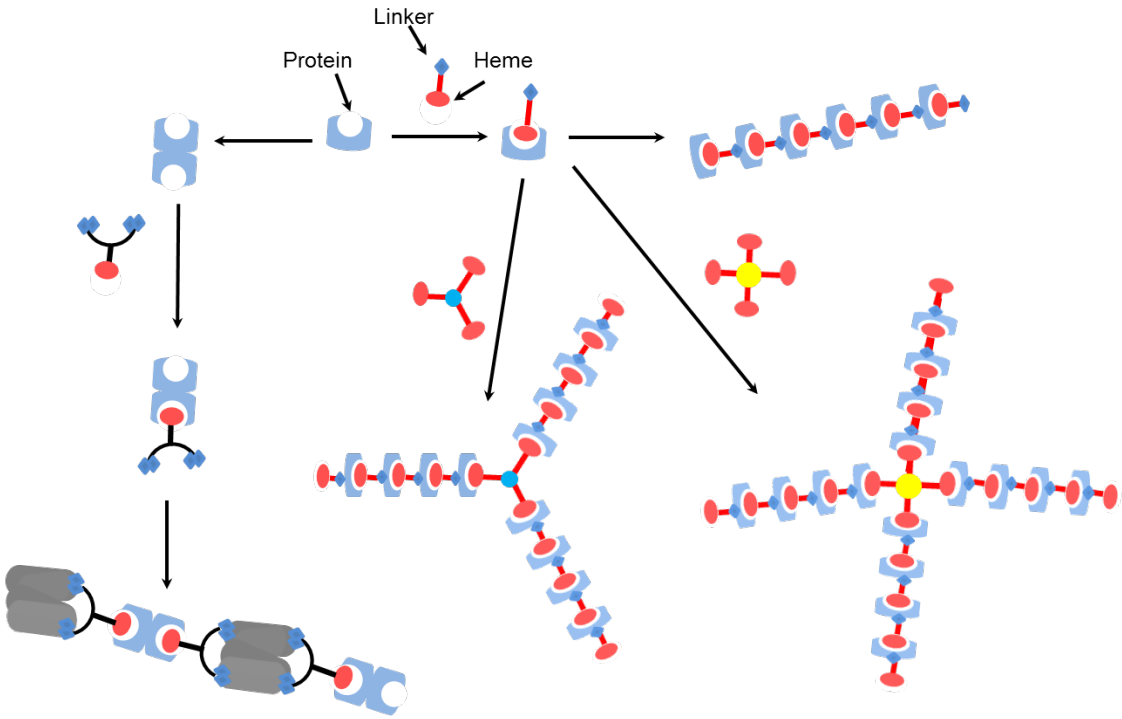

Figure 1.2 Schematic view of hemeprotein design with heme−heme pocket interaction.

However, the construction process of hemeprotein supramolecules by a chemical method (i.e., removing the heme from the natural protein and chemically attaching a heme to an unnatural position) is complex. Therefore, a new simple method for construction of hemeprotein supramolecules is desired.

1-2 Domain swapping

3D domain-swapping (i.e., simply, domain-swapping) is a phenomenon that has been observed in many proteins (*13-16*). Domain-swapping is a mechanism for forming oligomeric proteins from their monomers (Figure 1.3). In domain-swapping, one domain of a protein is replaced by the same domain from an identical protein, forming an intertwined dimer and high order oligomers. The first report on domain-swapping is the structure of diphtheria toxin dimer reported by Bennett and coworkers in 1994 (Figure 1.4a) (*17*).

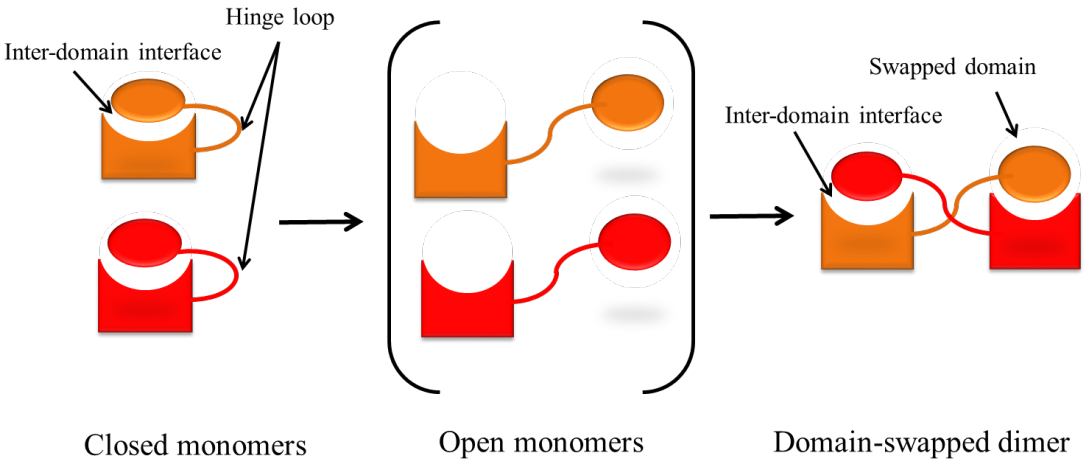

Figure 1.3 Schematic diagram of domain-swapping.

Up to date, many domain-swapped oligomeric proteins have been reported (*18-20*). The swapped domain can be as large as an entire globular domain as in diphtheria toxin (Figure 1.4a) (*17*). In cyanovirin-N (*21*), the swapped domain is half of

its molecule. The swapped domain can also be as small as an α-helix or a β-strand (*22*) as in the dimer of mouse Glucocorticoid-induced TNF receptor ligand (GITRL) (Figure 1.4b) (*23*). The swapped domains can be either the N terminus or the C terminus, or both of those (*13*). Some proteins form several domain-swapped structures. For example, ribonuclease A forms at least two domain-swapped oligomers (*24*), exchanging the N-terminal α-helix (*25*) and the C-terminal β-strand (*26*).

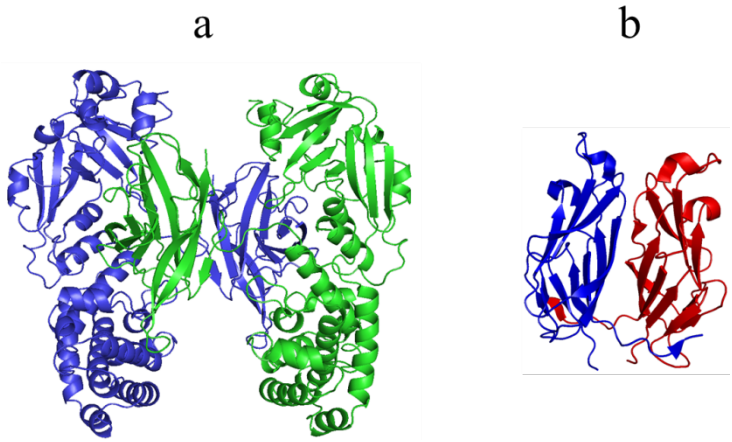

Figure 1.4 Protein structures formed by domain-swapping: (a) dimer of diphtheria toxin (PDB ID code: 1DDT), (b) dimer of mouse glucocorticoid-induced TNF receptor ligand (PDB ID code: 2Q8O).

Another structural characteristic in domain-swapping is a flexible hinge region. The hinge region links the two domains of the protomer. This is the only structural difference between the monomer and oligomers.

The hinge loop modification has been also used for protein design. Changes in

the hinge loop can promote the domain-swapping oligomerization. A very stable dimer can form by deletion of amino acids at the hinge loop (*27-29*). Deletion of six amino acids residues at a surface loop transformed staphylococcal nuclease transfers a monomeric protein into a very stable dimer (Figure 1.6a) (*29*). In p13suc1, the monomer–dimer equilibrium has been controlled by mutations of proline90 or proline92 at the hinge loop to alanine and changing the flexibility of the hinge loop (Figure 1.5) (*30*). Similar oligomerization phenomena have been observed in domain 1 of lymphocyte cell adhesion molecular CD2 (*31*), single-chain antibody variable fragment (scFv) (*32, 33*), eye lens beta-crystallin (*34*), and other proteins (*35-38*).

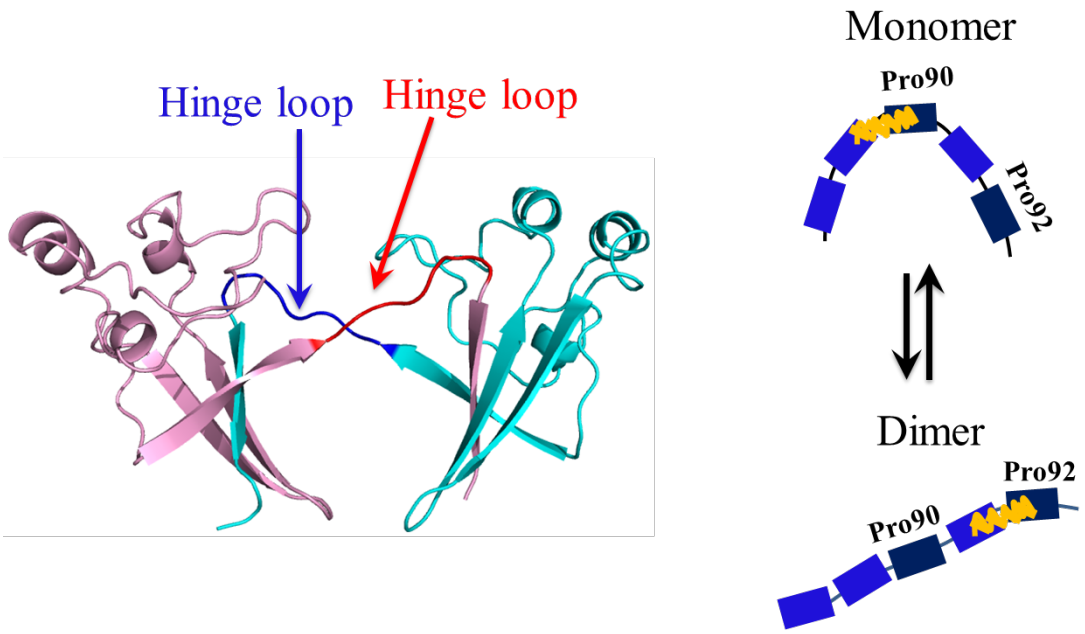

Figure 1.5 Protein structure of dimeric p13suc1 (PDB ID code: 1SCE).

Recently, our group has reported a hinge loop mutant of *Hydrogenobacter*

thermophilus (HT) cyt c_{552} (*39*). Insertion of three glycine residues at the hinge loop (between Ala18 and Lys19) reduced the steric hindrance in the domain-swapped oligomer, which increased the amount of high-order oligomers (Figure 1.6b). This result showed that the length and flexibility of the hinge loop affects the oligomerization of proteins, and domain-swapping can be utilized to design proteins.

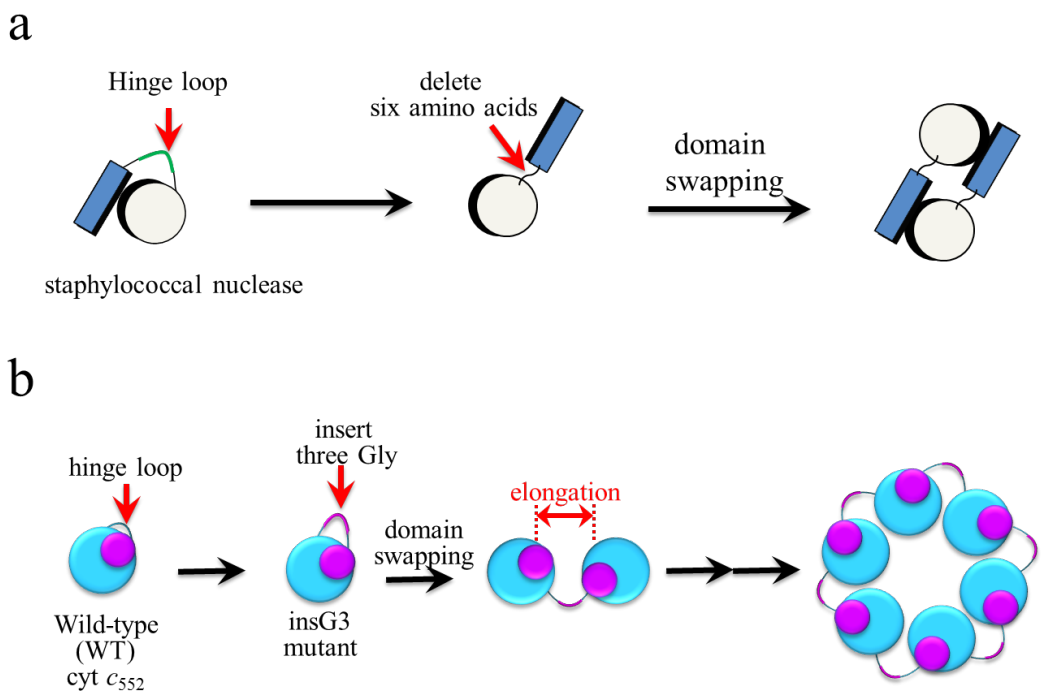

Figure 1.6 Schematic view of (a) deletion of six amino acids at the surface loop of *staphylococcal nuclease* for formation of a very stable dimer and (b) insertion of Gly residues between Ala18 and Lys19 at the hinge loop of cyt c_{552} for formation of high-order oligomers.

1-3 *c*-type cytochromes

1-3-1 Structure and function of cytochrome *c*

Cyt *c* is a globular protein with a heme covalently bound to the protein moiety (*40-42*). Cyt *c* transfers electrons form cytochrome bc_1 complex to cytochrome *c* oxidase in the respiratory chain of mitochondria, and also plays an important role in apoptosis. The molecular weight of horse cyt *c* is 12,400 Da. Its heme is covalently linked with Cysteine14 (Cys14) and Cys17 via two thioether bonds, and enveloped into a hydrophobic area in the protein interior. Two axial ligands, histidine18 (His18) and methionine80 (Met80) are coordinated to the heme iron (Figure 1.7).

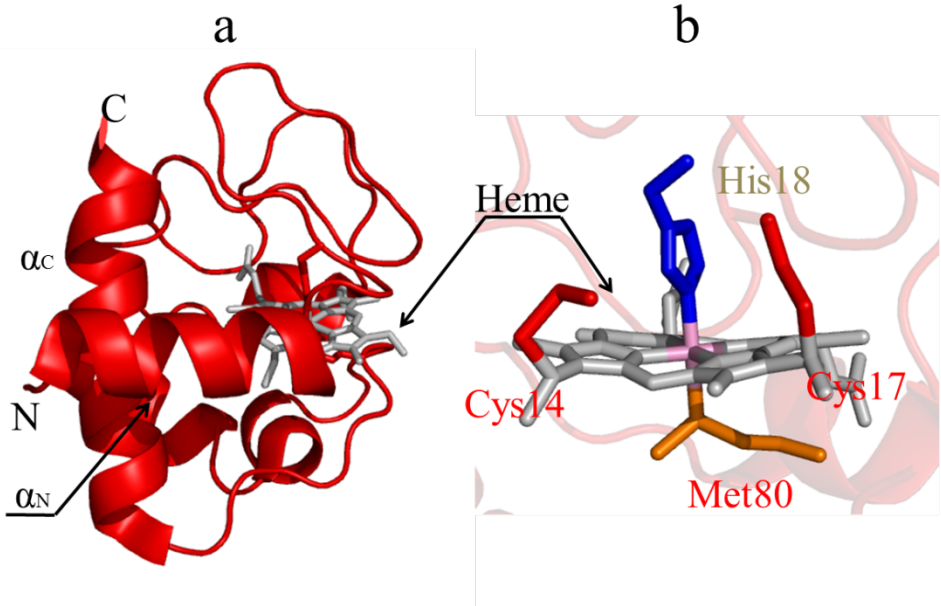

Figure 1.7 Structure of horse cyt *c* (PDB ID code: 1HRC): (a) protein structure and (b) active site structure. The heme is shown as a gray stick model. Side-chain atoms of His18 and Met80 are shown as stick models.

HT cyt c_{552} and *Pseudomonas aeruginosa* (PA) cyt c_{551} belong to the cyt *c* superfamily (Figure 1.8). His and Met (HT cyt c_{552}, His14 and Met59; PA cyt c_{551}, His16 and Met61) also coordinate to the heme iron (Figure 1.9). The amino acid sequence of PA cyt c_{551} (82 amino acids) matches 56% of that of HT cyt c_{552} (80 amino acids). However, the denaturation temperature (T_m) of PA cyt c_{551} is 82 °C, and that of HT cyt c_{552} is higher than 100 °C, owing to the dense packing by hydrophobic interactions (*43*).

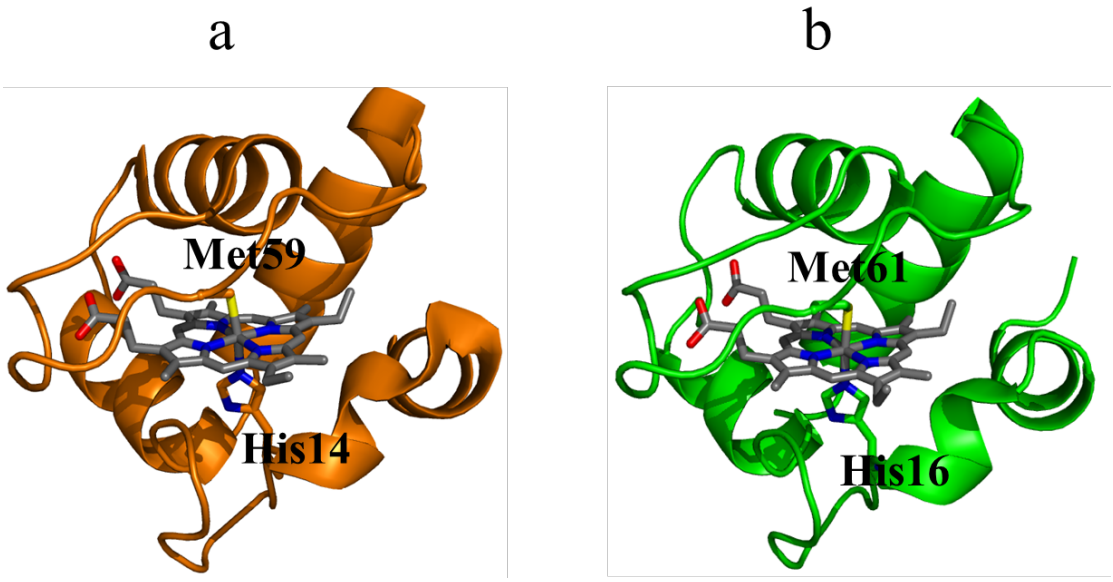

Figure 1.8 Protein structures of (a) HT cyt c_{552} (PDB ID code: 1YNR) and PA cyt c_{551} (PDB ID code: 351C). The hemes are shown as gray stick models. Side-chain atoms of heme-coordinating His and Met are shown as stick models.

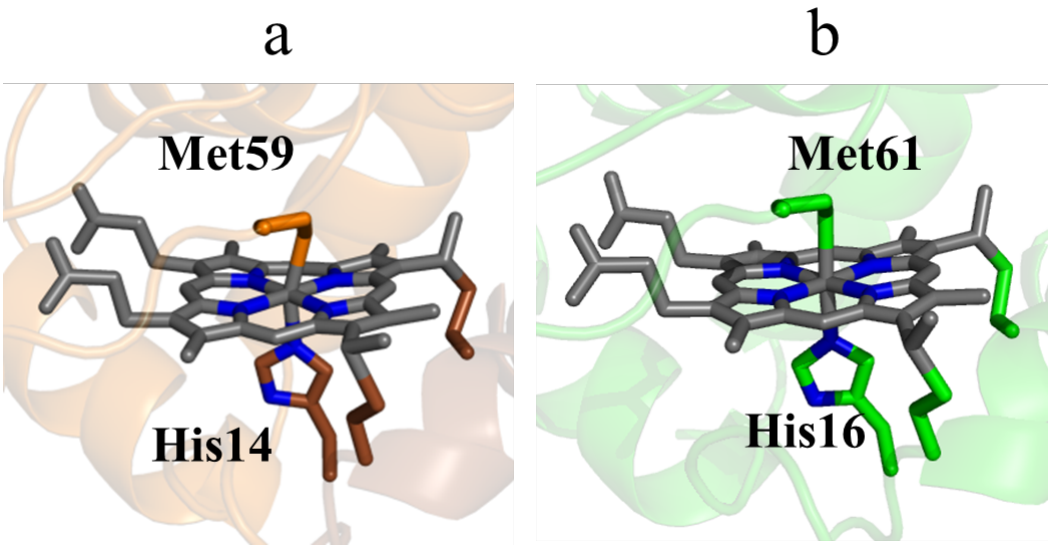

Figure 1.9 Active site structures of (a) HT cyt c_{552} (PDB ID code: 1YNR) and (b) PA cyt c_{551} (PDB ID code: 351C). The hemes are shown as gray stick models. Side-chain atoms of heme-coordinating His and Met are shown as stick models

1-3-2 Oligomerization of cytochrome *c*

It has been reported that horse cyt *c* forms oligomers by swapping its C-terminal helix domain successively (Figure 1.10) (*44*). The X-ray diffraction crystal structures of the cyt *c* dimer and trimer showed that the oligomers form closed-ended domain-swapped structures. Met80 was dissociated from the heme iron in the cyt *c* dimer and trimer (Figure 1.11). The peroxidase activity of dimeric cyt *c* was higher than that of the cyt *c* monomer, because the dissociation of Met80 created a binding site for hydrogen peroxide.

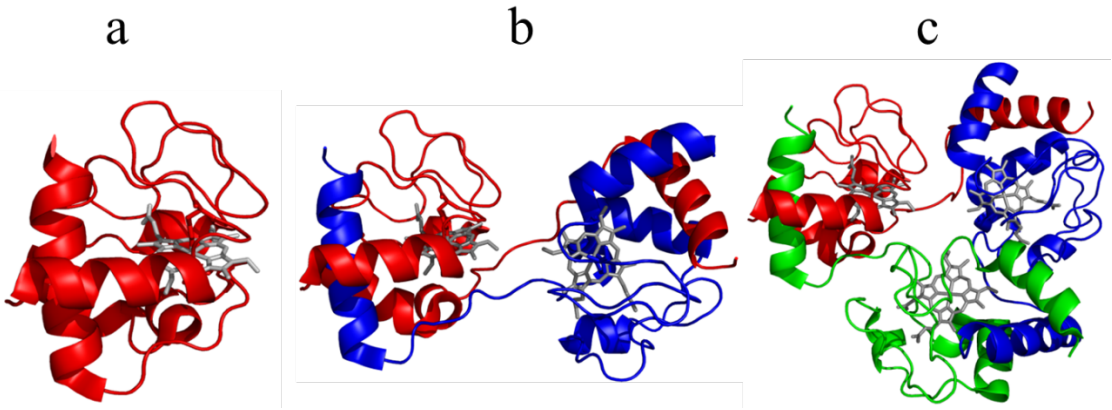

Figure 1.10 Protein structures of domain-swapped horse cyt *c* oligomers: (a) monomeric horse cyt *c* (PDB ID code: 1HRC), (b) dimeric horse cyt *c* (PDB ID code: 3NBS), (c) trimeric horse cyt *c* (PDB ID code: 3NBT). The hemes are shown as gray stick models.

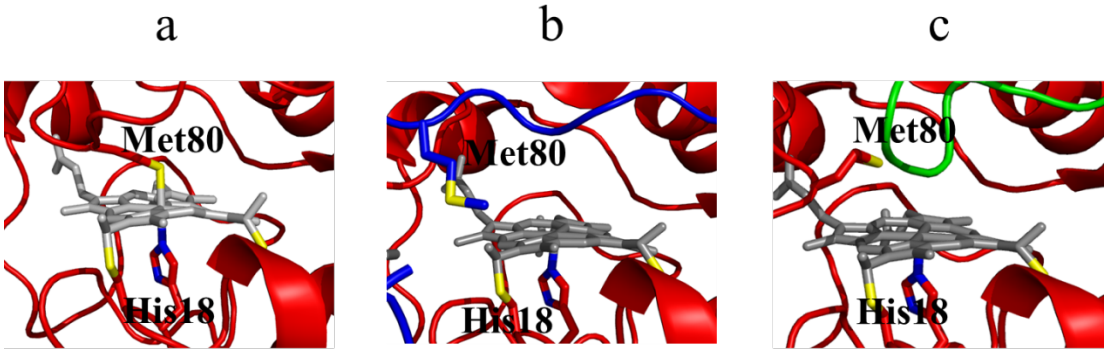

Figure 1.11 Active site structures of domain-swapped horse cyt *c* oligomers: (a) monomeric horse cyt *c* (PDB ID code: 1HRC), (b) dimeric horse cyt *c* (PDB ID code: 3NBS), and (c) trimeric horse cyt *c* (PDB ID code: 3NBT). The hemes are shown as gray stick models. Side-chain atoms of His18 and Met80 are shown as stick models.

HT cyt c_{552} and PA cyt c_{551} also form oligomers by domain-swapping. The dimer of HT cyt c_{552} formed by exchanging the region containing the N-terminal α-helix and heme (Figure 1.12) (*45, 46*), where the swapped region was different from that of

the horse cyt *c*. The hinge loop of dimeric HT cyt c_{552} was constructed with Ala18–Lys20. His14 and Met59 coordinated to the heme iron in dimeric HT cyt c_{552}, (Figure 1.13a), but the heme axial ligands belonged to different protomers. The structure of dimeric PA cyt c_{551} was also similar to that of dimeric HT cyt c_{552}, and the region containing the N-terminal helix and heme was exchanged between protomers (Figure 1.14). His and Met also coordinated to the heme iron in dimeric PA cyt c_{551} (Figure 1.13b).

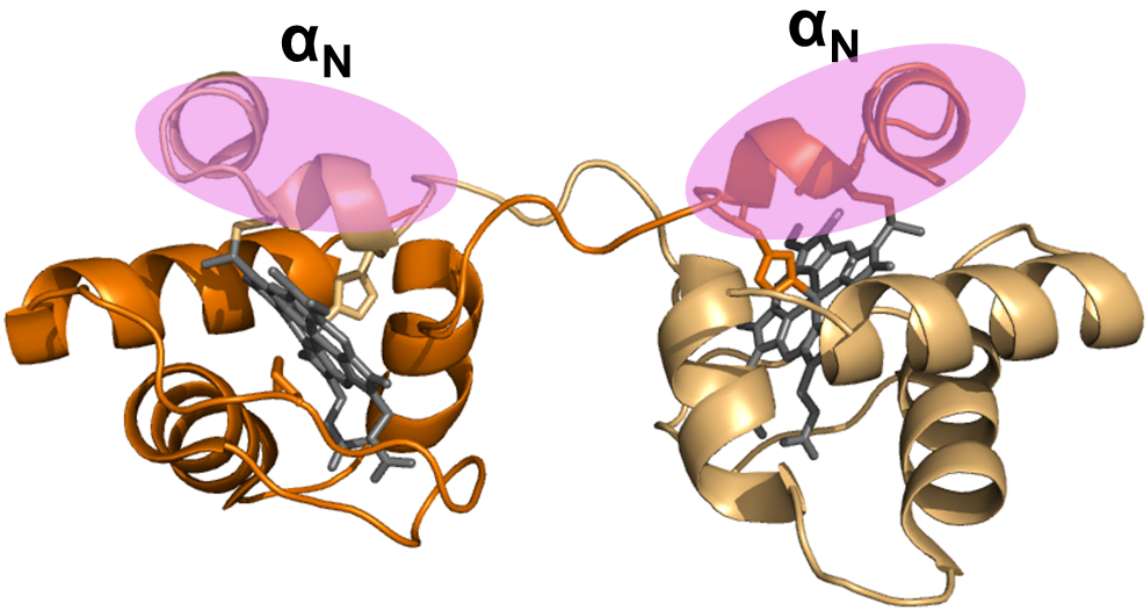

Figure 1.12 Protein structure of dimeric HT cyt c_{552} (PDB ID code: 3VYM). The hemes are shown as gray stick models. Each protomer is shown in brown or light brown. Side-chain atoms of His14 and Met59 are shown as stick models.

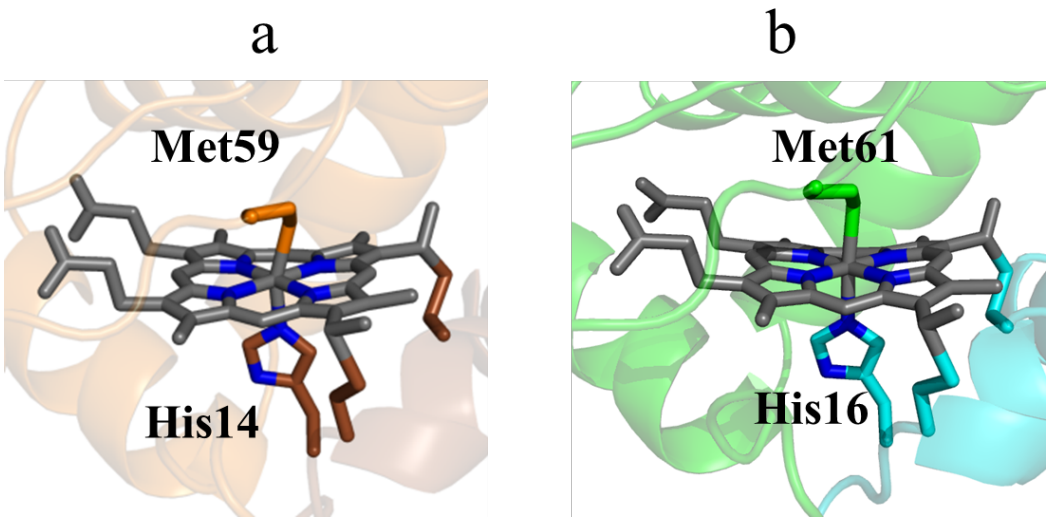

Figure 1.13 Active site structures of (a) dimeric HT cyt c_{552} (PDB ID code: 3VYM) and (b) dimeric PA cyt c_{551} (PDB ID code: 3X39). The hemes are shown in gray stick models. Each protomer is shown in brown or light brown for dimeric HT cyt c_{552}, and green and light blue for dimeric PA cyt c_{5521}. Side-chain atoms of heme-coordinating His and Met are shown as stick models.

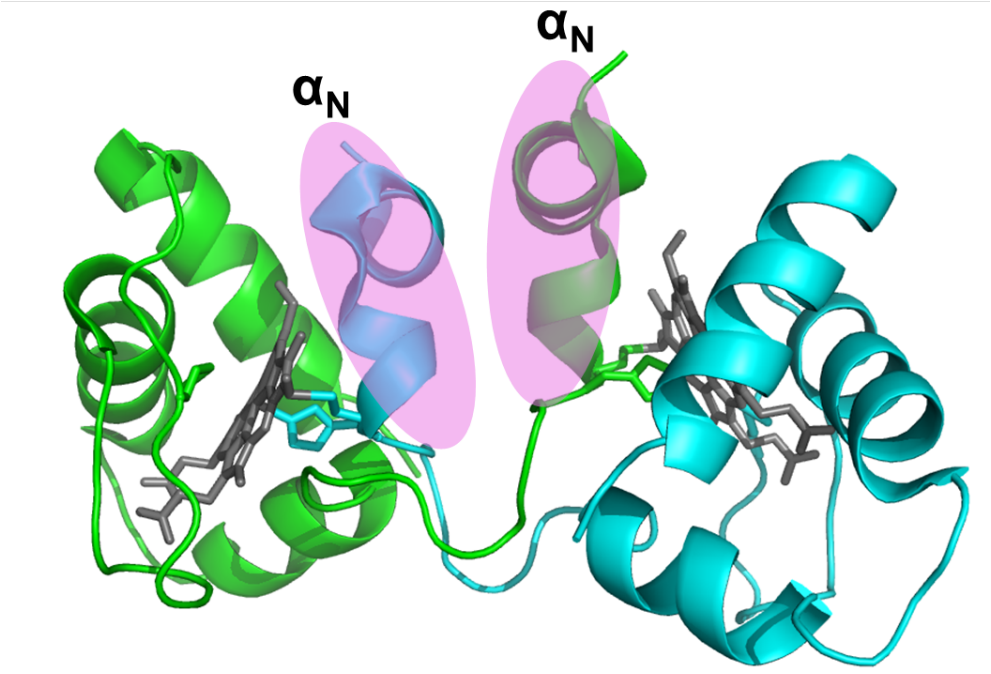

Figure 1.14 Protein structure of dimeric PA cyt c_{551} (PDB ID code: 3X39). The hemes are shown as gray stick models. Each protomer is shown in green or light blue. Heme-coordinating side-chain atoms of His16 and Met61 are shown as stick models.

1-3-3 Functional changes of cytochrome *c*

In cyt *c*, functional change by modification of its heme coordination has been reported (*47-49*). Removal of the heme-coordinating Met induces the reactivity of cyt *c* with external ligands. For example, peroxidase activity increases by Met dissociation from the heme iron (*50*). In addition, dimeric horse cyt *c* can bind cyanide ion due to Met80 dissociation from the heme iron (*51*). Removal of Val83 and Gly84 caused Met80 dissociation from the heme iron, and induced Met80 oxidation by the reaction of the heme with molecular oxygen in the presence of a reducing agent (Figure 1.15) (*52*).

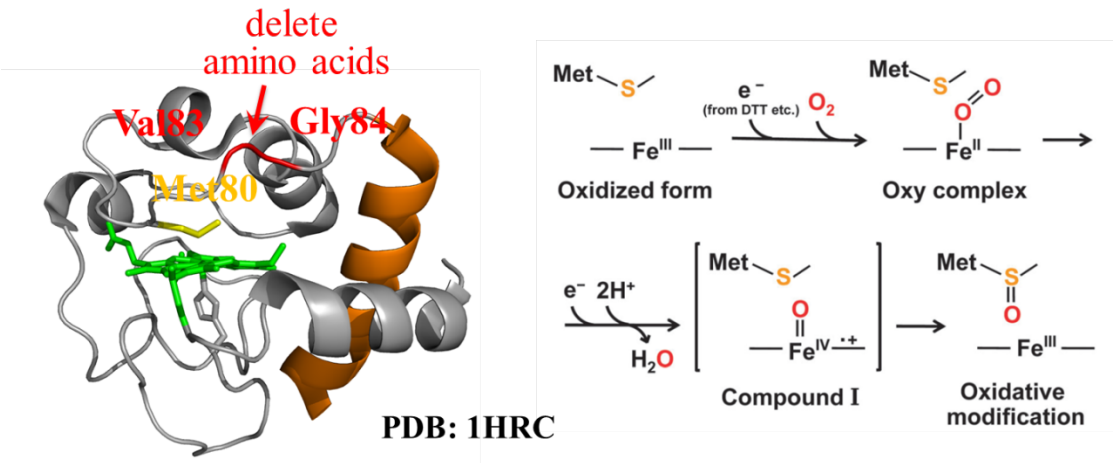

Figure 1.15 Structure of horse cyt *c* (PDB ID code: 1HRC) (left). The C-terminal α-helix is shown in brown. The heme is shown as a stick model. The deleted amino acids (Val83 and gly84), which caused Met80 dissociation from the heme iron, are shown in red. Met80 is shown in yellow. Putative reaction mechanism for its Met80 oxidation by formation of an oxygenated species and Compound I (right).

1-4 Purpose of this study

Cyt *c* forms oligomers by domain-swapping and changes its function by modification of the coordination structure at the heme active site. Replacement of heme-coordinating Met to Ala creates a binding site for external ligands. In this study, heterodimers with different active sites were constructed based on domain-swapping using Met-depleted *c*-type cytochromes (cyts). The structures of the heterodimers were determined by X-ray crystallography. To obtain functional insight into Met-depleted *c*-type cyts, the oxygen binding character of Met-depleted *c*-type cyt is investigated by resonance Raman spectroscopy.

1-5 References

1. Patterson, D. P., Su, M., Franzmann, T. M., Sciore, A., Skiniotis, G., Marsh, E. N. G. (2014) Characterization of a highly flexible self-assembling protein system designed to form nanocages, *Protein Sci. 23*, 190–199.

2. Whitesides, G. M., Boncheva, M. (2002) Beyond molecules: self-assembly of mesoscopic and macroscopic components, *Proc. Natl. Acad. Sci. U. S. A. 99*, 4769–4774.

3. Rudra, J. S., Collier, J. H., Ducheyne, P. (2011) Self-assembling biomaterials, In *Comprehensive Biomaterials*, pp 77–94, Elsevier, Oxford.

4. Parui, P. P., Deshpande, M. S., Nagao, S., Kamikubo, H., Komori, H., Higuchi, Y., Kataoka, M., Hirota, S. (2013) Formation of oligomeric cytochrome *c* during folding by intermolecular hydrophobic interaction between N- and C-terminal α-helices, *Biochemistry 52*, 8732–8744.

5. DeGrado, W. F., Summa, C. M., Pavone, V., Nastri, F., Lombardi, A. (1999) De novo design and structural characterization of proteins and metalloproteins, *Annu. Rev. Biochem. 68*, 779–819.

6. Onoda, A., Kakikura, Y., Uematsu, T., Kuwabata, S., Hayashi, T. (2012) Photocurrent generation from hierarchical zinc-substituted hemoprotein

assemblies immobilized on a gold electrode, *Angew. Chem. Int. Ed. 51*, 2628–2631.

7. Onoda, A., Takahashi, A., Oohora, K., Onuma, Y., Hayashi, T. (2012) Fibrous supramolecular hemoprotein assemblies connected with synthetic heme dimer and apohemoprotein dimer, *Chem. Biodivers. 9*, 1684–1692.

8. Onoda, A., Ueya, Y., Sakamoto, T., Uematsu, T., Hayashi, T. (2010) Supramolecular hemoprotein-gold nanoparticle conjugates, *Chem. Commun. 46*, 9107–9109.

9. Oohora, K., Hayashi, T. (2014) Hemoprotein-based supramolecular assembling systems, *Curr. Opin. Chem. Biol. 19*, 154–161.

10. Kitagishi, H., Kakikura, Y., Yamaguchi, H., Oohora, K., Harada, A., Hayashi, T. (2009) Self-assembly of one- and two-dimensional hemoprotein systems by polymerization through heme-heme pocket interactions, *Angew. Chem. Int. Ed. 48*, 1271–1274.

11. Kitagishi, H., Oohora, K., Yamaguchi, H., Sato, H., Matsuo, T., Harada, A., and Hayashi, T. (2007) Supramolecular hemoprotein linear assembly by successive interprotein heme−heme pocket interactions, *J. Am. Chem. Soc. 129*, 10326–10327.

12. Oohora, K., Burazerovic, S., Onoda, A., Wilson, Y. M., Ward, T. R., Hayashi, T. (2012) Chemically programmed supramolecular sssembly of hemoprotein and streptavidin with alternating alignment, *Angew. Chem. Int. Ed. 51*, 3818–3821.

13. Liu, Y., Eisenberg, D. (2002) 3D domain swapping: as domains continue to swap, *Protein Sci. 11*, 1285–1299.

14. Zerovnik, E., Stoka, V., Mirtic, A., Guncar, G., Grdadolnik, J., Staniforth, R. A., Turk, D., Turk, V. (2011) Mechanisms of amyloid fibril formation focus on domain swapping, *FEBS J. 278*, 2263–2282.

15. Bennett, M. J., Sawaya, M. R., Eisenberg, D. (2006) Deposition diseases and 3D domain swapping, *Structure 14*, 811–824.

16. Bennett, M. J., Schlunegger, M. P., Eisenberg, D. (1995) 3D domain swapping: a mechanism for oligomer assembly, *Protein Sci. 4*, 2455–2468.

17. Bennett, M. J., Choe, S., Eisenberg, D. (1994) Refined structure of dimeric diphtheria toxin at 2.0 Å resolution, *Protein Sci. 3*, 1444–1463.

18. Nagao, S., Osuka, H., Yamada, T., Uni, T., Shomura, Y., Imai, K., Higuchi, Y., Hirota, S. (2012) Structural and oxygen binding properties of dimeric horse myoglobin, *Dalton Trans. 41*, 11378–11385.

19. Miyamoto, T., Kuribayashi, M., Nagao, S., Shomura, Y., Higuchi, Y., Hirota, S.

(2015) Domain-swapped cytochrome cb_{562} dimer and its nanocage encapsulating a Zn–SO_4 cluster in the internal cavity, *Chem. Sci. 6*, 7336–7342.

20. Mazzarella, L., Capasso, S., Demasi, D., Di Lorenzo, G., Mattia, C. A., and Zagari, A. (1993) Bovine seminal ribonuclease: structure at 1.9 Å resolution, *Acta Crystallogr. D 49*, 389–402.

21. Yang, F., Bewley, C. A., Louis, J. M., Gustafson, K. R., Boyd, M. R., Gronenborn, A. M., Clore, G. M., Wlodawer, A. (1999) Crystal structure of cyanovirin-N, a potent HIV-inactivating protein, shows unexpected domain swapping 1, *J. Mol. Biol. 288*, 403–412.

22. Yamasaki, M., Li, W., Johnson, D. J. D., Huntington, J. A. (2008) Crystal structure of a stable dimer reveals the molecular basis of serpin polymerization, *Nature 455*, 1255–1258.

23. Zhou, Z., Tone, Y., Song, X., Furuuchi, K., Lear, J. D., Waldmann, H., Tone, M., Greene, M. I., Murali, R. (2008) Structural basis for ligand-mediated mouse GITR activation, *Proc. Natl. Acad. Sci. U. S. A. 105*, 641–645.

24. Libonati, M., Gotte, G. (2004) Oligomerization of bovine ribonuclease A: structural and functional features of its multimers, *Biochem. Soc. 380*, 311–327.

25. Liu, Y., Hart, P. J., Schlunegger, M. P., Eisenberg, D. (1998) The crystal

structure of a 3D domain-swapped dimer of RNase A at a 2.1 Å resolution, *Proc. Natl. Acad. Sci. U. S. A. 95*, 3437–3442.

26. Liu, Y., Gotte, G., Libonati, M., Eisenberg, D. (2001) A domain-swapped RNase A dimer with implications for amyloid formation, *Nat. Struct. Mol. Biol. 8*, 211–214.

27. Ogihara, N. L., Ghirlanda, G., Bryson, J. W., Gingery, M., DeGrado, W. F., Eisenberg, D. (2001) Design of three-dimensional domain-swapped dimers and fibrous oligomers, *Proc. Natl. Acad. Sci. U. S. A. 98*, 1404–1409.

28. Pei, X., Holliger, P., Murzin, A. G., Williams, R. L. (1997) The 2.0 Å resolution crystal structure of a trimeric antibody fragment with noncognate V_H-V_L domain pairs shows a rearrangement of V_H CDR3, *Proc. NatL. Acad. Sci. U. S. A. 94*, 9637–9642.

29. Green, S. M., Gittis, A. G., Meeker, A. K., Lattman, E. E. (1995) One-step evolution of a dimer from a monomeric protein, *Nat. Struct. Mol. Biol. 2*, 746–751.

30. Rousseau, F., Schymkowitz, J. W. H., Wilkinson, H. R., Itzhaki, L. S. (2001) Three-dimensional domain swapping in p13suc1 occurs in the unfolded state and is controlled by conserved proline residues, *Proc. Natl. Acad. Sci., U. S. A.*

98, 5596–5601.

31. Murray, A. J., Lewis, S. J., Barclay, A. N., Brady, R. L. (1995) One sequence, two folds: a metastable structure of CD2, *Proc. Natl. Acad. Sci. U. S. A. 92*, 7337–7341.

32. Kortt, A. A., Malby, R. L., Caldwell, J. B., Gruen, L. C., Ivancic, N., Lawrence, M. C., Howlett, G. J., Webster, R. G., Hudson, P. J., Colman, P. M. (1994) Recombinant anti-sialidase single-chain variable fragment antibody, *Eur. J. Biochem. 221*, 151–157.

33. Olga, P., Philip, A, W., Philipp, H., Greg, W., Roger, W. L. (1994) Crystal structure of a diabody, a bivalent antibody fragment, *Structure 2*, 1217–1226.

34. Lapatto, R., Nalini, V., Bax, B., Driessen, H., Lindley, P. F., Blundell, T. L., Slingsby, C. (1991) High resolution structure of an oligomeric eye lens β-crystallin. loops, arches, linkers and interfaces in β_2 dimer compared to a monomeric gamma-crystallin, *J. Mol. Biol. 222*, 1067–1083.

35. Albright, R. A., Mossing, M. C., Matthews, B. W. (1996) High-resolution structure of an engineered Cro monomer shows changes in conformation relative to the native dimer, *Biochemistry 35*, 735–742.

36. Kuhlman, B., O'Neill, J. W., Kim, D. E., Zhang, K., Baker, D. (2001)

Conversion of monomeric protein L to an obligate dimer by computational protein design, *Proc. Natl. Acad. Sci. U. S. A. 98*, 10687–10691.

37. O'Neill, J. W., Kim, D. E., Baker, D., Zhang, K. Y. (2001) Structures of the B1 domain of protein L from *Peptostreptococcus magnus* with a tyrosine to tryptophan substitution, *Acta Crystallogr. D 57*, 480–487.

38. Trinkl, S., Glockshuber, R., Jaenicke, R. (1994) Dimerization of beta B2-crystallin: the role of the linker peptide and the N- and C-terminal extensions, *Protein Sci. 3*, 1392–1400.

39. Ren, C., Nagao, S., Yamanaka, M., Komori, H., Shomura, Y., Higuchi, Y., Hirota, S. (2005) Oligomerization enhancement and two domain swapping mode detection for thermostable cytochrome c_{552} *via* the elongation of the major hinge loop, *Mol. BioSyst. 11*, 3218–3221

40. Bushnell, G. W., Louie, G. V., Brayer, G. D. (1990) High-resolution three-dimensional structure of horse heart cytochrome *c*, *J. Mol. Biol. 214*, 585–595.

41. Dickerson, R. E., Takano, T., Eisenberg, D., Kallai, O. B., Samson, L., Cooper, A., Margoliash, E. (1971) Ferricytochrome *c*, *J. Biol. Chem. 246*, 1511–1535.

42. Mandel, N., Mandel, G., Trus, B. L., Rosenberg, J., Carlson, G., Dickerson, R. E.

(1977) Tuna cytochrome *c* at 2.0 Å resolution, *J. Biol. Chem. 252*, 4619–4636.

43. Uchiyama, S., Ohshima, A., Nakamura, S., Hasegawa, J., Terui, N., Takayama, S. J., Yamamoto, Y., Sambongi, Y., Kobayashi, Y. (2004) Complete thermal-unfolding profiles of oxidized and reduced cytochromes *c, J. Am. Chem. Soc. 126*, 14684–14685.

44. Hirota, S., Hattori, Y., Nagao, S., Taketa, M., Komori, H., Kamikubo, H., Wang, Z., Takahashi, I., Negi, S., Sugiura, Y., Kataoka, M., Higuchi, Y. (2010) Cytochrome *c* polymerization by successive domain swapping at the C-terminal helix, *Proc. Natl. Acad. Sci. U. S. A. 107*, 12854–12859.

45. Nagao, S., Ueda, M., Osuka, H., Komori, H., Kamikubo, H., Kataoka, M., Higuchi, Y., Hirota, S. (2015) Domain-swapped dimer of *Pseudomonas aeruginosa* cytochrome c_{551}: structural insights into domain swapping of cytochrome *c* family proteins, *PLoS ONE 10*, e0123653.

46. Hayashi, Y., Nagao, S., Osuka, H., Komori, H., Higuchi, Y., Hirota, S. (2012) Domain swapping of the heme and N-terminal α-helix in *Hydrogenobacter thermophilus* cytochrome c_{552} dimer, *Biochemistry 51*, 8608–8616.

47. Dolla, A., Florens, L., Bianco, P., Haladjian, J., Voordouw, G., Forest, E., Wall, J., Guerlesquin, F., Bruschi, M. (1994) Characterization and oxidoreduction

properties of cytochrome c_3 after heme axial ligand replacements, *J. Biol. Chem. 269*, 6340–6346.

48. Mauk, A. G., Moore, G. R. (1997) Control of metalloprotein redox potentials: what does site-directed mutagenesis of hemoproteins tell us?, *J. Biol. Inorg. Chem. 1*, 119–125

49. Mus, V. I., Dolla, A., Guerlesquin, F., Payan, F., Czjzek, M., Haser, R., Bianco, P., Haladjian, J., Rapp-Giles, B J., Wall, J D. (1992) Site-directed mutagenesis of tetraheme cytochrome c_3. modification of oxidoreduction potentials after heme axial ligand replacement, *J. Biol. Chem. 267*, 16851–16858.

50. Wang, Z., Matsuo, T., Nagao, S., Hirota, S. (2011) Peroxidase activity enhancement of horse cytochrome *c* by dimerization, *Org. Biomol. Chem. 9*, 4766–4769.

51. Nugraheni. A. D., Nagao, S., Yanagisawa, S., Ogura, T., Hirota, S. (2013) Interaction of dimeric horse cytochrome *c* with cyanide ion, *J. Inorg. Chem. 18* 383–390

52. Wang, Z., Ando, Y., Nugraheni, A. D., Ren, C., Nagao, S., Hirota, S. (2014) Self-oxidation of cytochrome c at methionine80 with molecular oxygen induced by cleavage of the Met-heme iron bond, Mol. BioSyst. 10, 3130–3137.

Chapter 2

Construction of *c*-type cytochrome heterodimers with different active sites

Section 2-1

Construction of heterodimer with different active sites using *c*-type HT wild-type cyt c_{552} and its mutant

2-1-1 Introduction

Myoglobin (Mb) has been shown to domain swap and forms a dimer (*1*). Recently, our group has reported a Mb heterodimer with two different active sites by controlling the salt bridges sites at the protomer interface of the domain-swapped dimer (*2*). In the wild-type Mb dimer, four salt bridges are formed at the surface of the protomers. We designed two mutants; one mutant with only positive residues at the hinge loop and the other mutant with only negative residues at the hinge loop. In addition, the heme active site was modified to a bis–His coordination site for the mutant with a positive interface. These two mutants formed a heterodimer with different active sites by domain-swapping. This result proposed a new example for rational protein design base on domain-swapping.

In this study, I extended this concept to *c*-type cytochrome. I used HT cyt c_{552}. Met59, which coordinates to the heme iron, was replaced with Ala in HT cyt c_{552} (M59A cyt c_{552}) to allow external ligands to bind to the heme iron. Then, I constructed a heterodimer with different active sites by domain-swapping wild-type cyt c_{552} and mutant M59A cyt c_{552} (Figure 2.1).

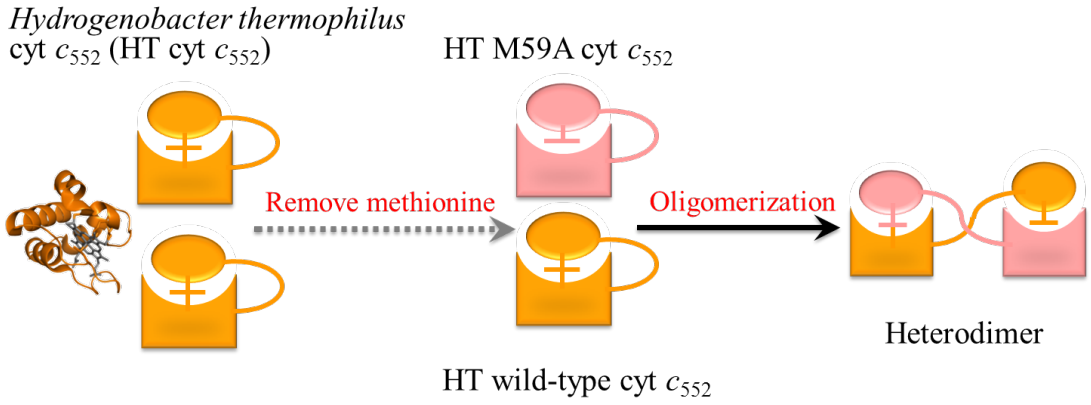

Figure 2.1 Design strategy for construction of the HT wild-type–M59A cyt c_{552} heterodimer.

2-1-2 Materials and methods

2-1-2-1 Plasmids for HT wild-type cyt c_{552} and HT mutant M59A cyt c_{552}

Plasmid pKO2 was used for expression of HT wild-type cyt c_{552}. Met59 of HT cyt c_{552} was substituted with Ala (HT M59A cyt c_{552}). Point mutation of Met to Ala was introduced into pKO2 by PCR-based *in vitro* mutagenesis using forward and reverse primers (Eurofins genomics) (Table 2.1) and Primer STAR max DNA polymerase (Takara Bio). Plasmid DNA was prepared using *Escherichia coli* (*E.coli*) DH5α cells, and purified with QIAprep spin Mini prep kit (Qiagen). DNA sequencing was conducted with the BigDye Terminator version 3.1 cycle sequencing kit (Applied Biosystems, Inc., Foster City, CA) and an ABI PRISM 3100 genetic analyzer sequencing system (Applied Biosystems, Inc.). The constructed plasmid was introduced into *E.coli* JCB387 cells containing the PEC86 plasmid DNA.

2-1-2-2 Purification of HT wild-type cyt c_{552} and HT M59A cyt c_{552}

HT wild-type cyt c_{552} and HT M59A cyt c_{552} were overproduced in *E. coli* JCB387 cells. The *E. coli* cells were grown aerobically in 25 g/L LB broth at 37 °C until OD_{600} reached around 1.5, and then harvested by centrifugation (8,000 g, 5 min, 4 °C). After centrifugation, the cells were suspended in spheroplasting buffer (100 mM

Tris-HCl buffer, pH 8.0, containing 10 mM EDTA and 20 % (w/v) sucrose) to extract periplasmic protein by the osmotic method. Suspended cells were incubated on ice for 30 min, and then centrifuged (13,700 g, 30 min, 4 °C). The resulting supernatant was collected. The cells were suspended again in pure water and incubated on ice for 30 min. After centrifugation (13,700 g, 30 min, 4 °C), the supernatant was collected and added to the supernatant obtained in the previous step. The protein solution was dialyzed overnight at 4 °C with 25 mM sodium acetate buffer, pH 5.0. The proteins were oxidized by an addition of excess (~10 fold) potassium ferricyanide. The proteins in 25 mM sodium acetate buffer, pH5.0, were purified by cation exchange chromatography (CM-cellulose column (Wako), HiTrap SP column (GE healthcare)) with a gradient of 0 to 300 mM NaCl. Subsequently, the proteins were purified by size exclusion chromatography (HiLoad 26/60 Superdex 75, GE healthcare) using a fast protein liquid chromatography (FPLC) system (BioLogic DuoFlow 10, Bio-Rad, CA) at 4 °C with 50 mM potassium phosphate buffer, pH 7.0.

The molar extinction coefficient of HT M59A cyt c_{552} protein was obtained with the pyridine hemochrome method (ε = 160,000 ± 2000 $M^{-1}cm^{-1}$ at 401 nm) (*3*). The concentration of the monomer was calculated from the absorbance at 401 nm with the absorption coefficient.

2-1-2-3 Oligomerization of HT wild-type–M59A cyt c_{552} heterodimer

HT wild-type cyt c_{552} and HT M59A cyt c_{552} were mixed with 1:1 molar ratio in 50 mM potassium phosphate buffer, pH 7.0. Ethanol was added to the mixture solution at 50 °C as a final concentration of 80 % (v/v). The resulting precipitate was separated from the supernatant by centrifugation at 10,000 g for 10 min. The obtained precipitate was lyophilized to remove the residual ethanol and then dissolved with 2 mL of 50 mM potassium phosphate buffer, pH 7.0, at 4 °C. The dimers were separated by size exclusion chromatography (HiLoad 26/60 Superdex 75, GE healthcare) using the FPLC system (BioLogic DuoFlow 10, Bio-Rad, CA) at a flow rate of 1.0 mL/min at 4 °C. The fraction containing dimers was incubated at 75 °C for 3 hrs to allow dissociation of the mutant M59A cyt c_{552} homodimer. The mutant M59A cyt c_{552} homodimer is unstable because of the loss the bond between the heme and Met. The dimer fraction was collected for further purification to separate the heterodimer from the wild-type cyt c_{552} homodimer. The solution of heterodimer and wild-type cyt c_{552} homodimer mixture was reduced by a mild reducing agent, ascorbic acid (~5 fold). The His/Met-coordinated site is reduced by ascorbic acid, but the His/H_2O-coordinated site can not be reduced by ascorbic acid. The heterodimer contained two active sites, one His/Met-coordination and one His/H_2O-coordination. On the other hand, the wild-type cyt c_{552} homodimer

contained two His/Met-coordination sites. The heterodimer was reduced for a single charge, whereas the wild-type homodimer was reduced by two charges. This charge difference allowed to separate the two dimers by ion exchange chromatography. After removal of ascorbic acid by a PD-10 desalting column (GE healthcare), the dimers were purified by a Mono S^{TM} 5/50 GL column (GE healthcare) using the FPLC system with 10 mM potassium phosphate buffer, pH 7.0, at a flow rate of 0.5 mL/min at 4 °C. The fractions containing the dimers were eluted with a gradient of 55−75 mM Na_2SO_4 over a period of 80 min. The cation exchange chromatography (Mono S^{TM} 5/50 GL column) was performed again to purify the heterodimer.

The molar extinction coefficient of the heterodimer was obtained by the pyridine hemochrome method (236,000 ± 1500 $M^{-1}cm^{-1}$ at 402.5 nm) (*3*). The concentration of the heterodimer was calculated from the absorbance at 402.5 nm with the absorption coefficient.

2-1-2-4 MALDI-TOF mass measurement

The buffer of protein solutions was changed to pure water by ultra filtration using Amicon Ultra (MWCO 3000, Millipore). MALDI-TOF mass spectrum of heterodimer was obtained with an Autoflex II mass spectrometer (Bruker Daltonics) in

linear mode using sinapinic acid as a matrix.

2-1-2-5 Optical absorption spectra and circular dichroism (CD) measurements

UV-2450 spectrophotometer (Shimadzu, Japan) and J-725 CD spectropolarimeter (Jasco, Japan) were used for optical absorption and CD measurements, respectively. 1-cm-path-length and 0.1-cm-path-length quartz cells were used for optical absorption and CD measurements, respectively.

2-1-2-6 Stability measurement of heterodimer

The stability of the heterodimer was measured by incubation of the heterodimer solution for 30 min at various temperatures (70 to 90 °C), and then analyzed by size exclusion chromatography (Superdex 75 10/300 GL) using the FPLC system (BioLogic DuoFlow 10, Bio-Rad, CA) with 50 mM potassium phosphate buffer, pH 7.0, at a flow rate of 0.5 mL/min at 4 °C.

2-1-2-7 Reduction potential measurement

Cyclic voltammetry responses were conducted with an ALS-612DN electrochemical analyzer (BAS Inc., Tokyo, Japan). An Au electrode acted as a working

electrode. A Pt wire and Ag/AgCl (3 M NaCl) were used as counter and reference electrodes, respectively. The collected data of potentials were referred to normal hydrogen electrode (NHE). The modification of the surface of the Au electrode was performed by the following procedure (*4*). The working Au electrode was rinsed with ethanol and pure water. Subsequently, the electrode was polished with 0.05 μm alumina water slurry. The electrode surface was rinsed with pure water to remove residual adsorbed impurities. Then the electrode was cleaned by electrochemical oxidation/reduction treatment (*5*). The Au electrode surface was modified by dipping the electrode in to a 1 mM 4-mercaptopyridine water solution for 30 seconds and rinsed with pure water. Cyclic voltammograms were recorded in 50 mM potassium phosphate buffer, pH 7.0, containing 200 mM NaCl. Each sample (monomers, 0.1 mM (heme unit); heterodimer, 0.2 mM (heme unit)) was degassed and flowed argon gas for at least 5 min to remove oxygen from the protein solution. The measurements were performed at room temperature at least three times.

2-1-2-8 X-ray crystallographic analysis

Crystals of HT wild-type–M59A cyt c_{552} heterodimer was obtained by the sitting drop vapor diffusion method with crystal plates (CrystalClear D Strips, Douglas

Instruments, Hampton Research, CA). Oxidized heterodimer was dissolved in 10 mM HEPES buffer, pH 7.0. The protein concentration of the heterodimer was 19.2 mg/mL. Droplets were prepared by mixing 1 μL of the heterodimer solution with 1 μL reservoir solution and were equilibrated. The best reservoir solution was found to be 1.6 M sodium citrate tribasic dehydrate, pH 6.5. A crystal was observed after incubation at 25 °C for four days.

The diffraction data were collected at the BL26B1 beamline of SPring-8 (Japan) for heterodimer using a MX225HE (Rayonix). The crystal was mounted on a cryo-loop and flash-frozen at 100 K in a nitrogen cryo system. The crystal-to-detector distance was 180 mm, and the wavelength was 1.0000 Å. The oscillation angle was 1.0°, and the exposure time was 5 s per frame. The total number of frames was 180. The diffraction data were processed using the program HKL2000 (*6*).

The preliminary structure was obtained by a molecular replacement programs using the atomic coordinates of the structure of monomeric HT wild-type cyt c_{552} (PDB code: 1YNR) as a starting model for the heterodimer.

The structure refinement was performed using the program, REFMAC (*7, 8*). The molecular model was manually corrected, and water molecules were picked up in the electron density map using the program, COOT (*9*). The data collection and

refinement statistics of the heterodimer is summarized in Table 2.2.

Table 2.1 Nucleotide sequences of primers.

Primer	Sequence[a]
HT-M59A-fw	GTTCCCGCGCCTCCTCAAAATGTAACCG
HT-M59A-rv	AGGAGGCGCGGGAACAGAACCCCACAC

[a]Underlines indicate the nucleotides for the modified amino acid

Table 2.2 Statistics of data collection and structure refinement of heterodimeric HT wild-type−M59A cyt c_{552}.

Data collection			
X-ray source	SPring-8 (BL26B1)		
Wavelength (Å)	1.0000		
Space group	$C222_1$		
Unit cell parameters			
a, b, c (Å)	63.4	115.1	83.2
α, β, γ (°)	90.0	90.0	90.0
Resolution (Å)	50.0−1.80 (1.83−1.80)		
Number of unique reflections	29399 (1549)		
R_{merge}[a]	0.070 (0.718)		
Completeness (%)	100.0 (99.8)		
$\langle I/\sigma(I)\rangle$	34.3 (3.0)		
$CC_{1/2}$	0.999 (0.875)		
Redundancy	7.2 (6.6)		
Refinement			
Resolution (Å)	50.0−1.80 (1.85−1.80)		
Number of reflections	26998 (2009)		
R_{work}[b]	0.2233 (0.278)		
R_{free}[b]	0.2533 (0.306)		
Completeness (%)	99.7 (96.7)		
Number of atoms in an asymmetric unit			
Protein	1819		
Water	79		
Heme	128		
Average B factors (Å^2)			
Protein	36.6		
Water	29.0		
Heme	25.7		
Ramachandran plot (%)			
Favored	100.0		
Allowed	0		
Outlier	0		

Statistics for the highest-resolution shell are given in parentheses.

[a] $R_{merge}=\Sigma_{hkl} | I- \langle I\rangle | (\Sigma_{hkl}| I |)^{-1}$.

[b] $R_{work}=\Sigma_{hkl} | | F_{obs} | - k| F_{calc} | | (\Sigma_{hkl} | F_{obs} |)^{-1}$, k: scaling factor. R_{free} was computed identically, except where all reflections belong to a test set of 5 % of randomly selected data.

2-1-3 Results and discussion

Oligomers formed by an addition of 80 % (v/v) ethanol at 50 °C to a mixture of HT wild-type cyt c_{552} and mutant M59A cyt c_{552}. The oligomers were separated by size exclusion chromatography (Figure 2.2). The peak correspond to the dimer was obtained in the size exclusion chromatogram. The peaks correspond to high order oligomers were also observed as is the case of HT wild-type cyt c_{552} oligomerization (*4*). The dimer fraction was further purified by cation exchange chromatography (Mono S^{TM} 5/50 GL column) (Figure 2.3). The observation of several peaks in the Mono S chromatogram indicate that the dimer fraction includes several dimer forms, i.e., the heterodimer and homodimers. Each peak in the chromatogram was analyzed by MALDI-TOF mass spectrometry. The mass spectrum of the fraction at 33–38 mL is shown in Figure 2.4. The mass spectrum showed two peaks at m/z 9189 and m/z 9128. These peaks at 9189 and 9128 corresponded well to theoretical molecular weights of positively charged wild-type cyt c_{552} and mutant M59A cyt c_{552}, respectively. These results indicate that HT wild-type cyt c_{552} and M59A cyt c_{552} constructed the dimer.

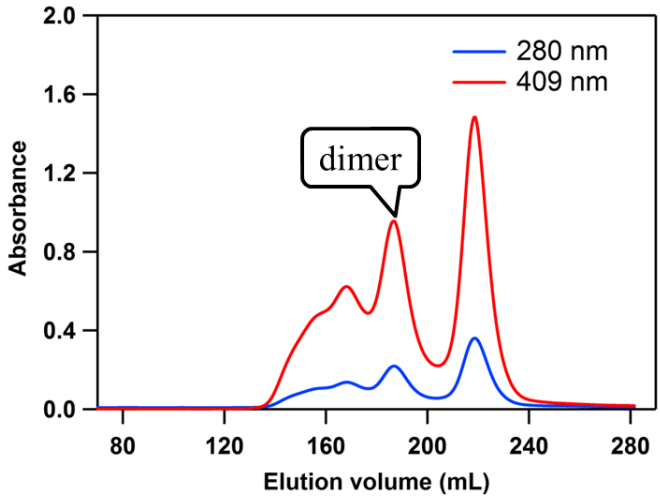

Figure 2.2 Size exclusion chromatogram of HT wild-type–M59A cyt c_{552} oligomer. Measurement conditions: column, HiLoad 26/60 Superdex 75; flow rate, 1.0 mL/min; monitoring wavelength, 280 nm (blue) and 409 nm (red); solvent, 50 mM potassium phosphate buffer (pH 7.0); temperature, 4 °C.

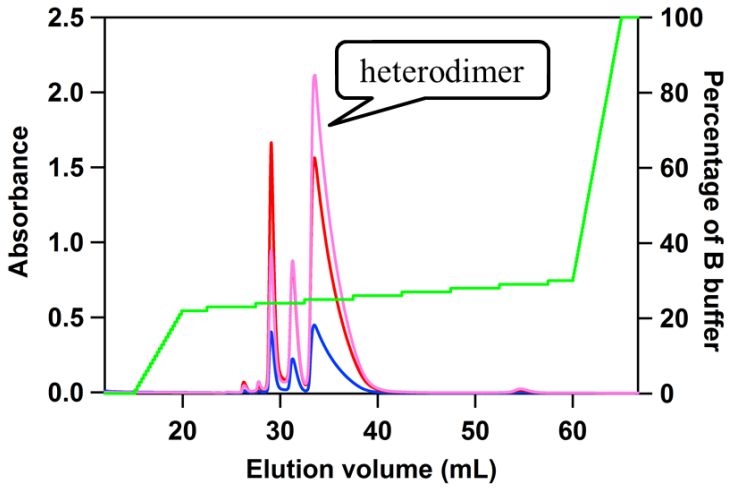

Figure 2.3 Cation exchange chromatogram of HT wild-type–M59A cyt c_{552} heterodimer. Measurement conditions: column, Mono S^{TM} 5/50 GL column; flow rate, 0.5 mL/min; monitoring wavelength, 280 nm (blue), 403 nm (pink) and 409 nm (red); solvent, buffer A: 10 mM potassium phosphate buffer (pH 7.0) and buffer B: 10 mM potassium phosphate buffer (pH 7.0), containing 250 mM Na_2SO_4; gradient 22–30 % of B buffer over a period of 80 min (green); temperature, 4 °C.

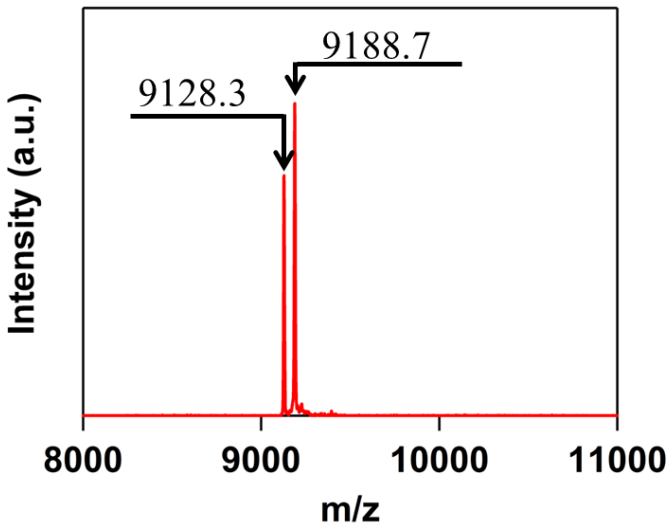

Figure 2.4 MALDI-TOF mass spectrum of the purified HT wild-type and M59A cyt c_{552} heterodimer. Measurement conditions: solvent, pure water; matrix, sinapinic acid.

To investigate the stability, the HT wild-type cyt c_{552}–M59A cyt c_{552} heterodimer was incubated for 30 min at various temperatures between 70 to 90 °C (Figure 2.5). The heterodimer dissociated to monomers by the incubation higher than 80 °C. The temperature for dissociation of wild-type cyt c_{552} homodimer was 90 °C (*4*). Thus, the dissociation temperature of the cyt *c* heterodimer was a little lower than that of the wild-type homodimer. These results suggest that the ligation of Met to the heme iron stabilizes the domain-swapped dimer.

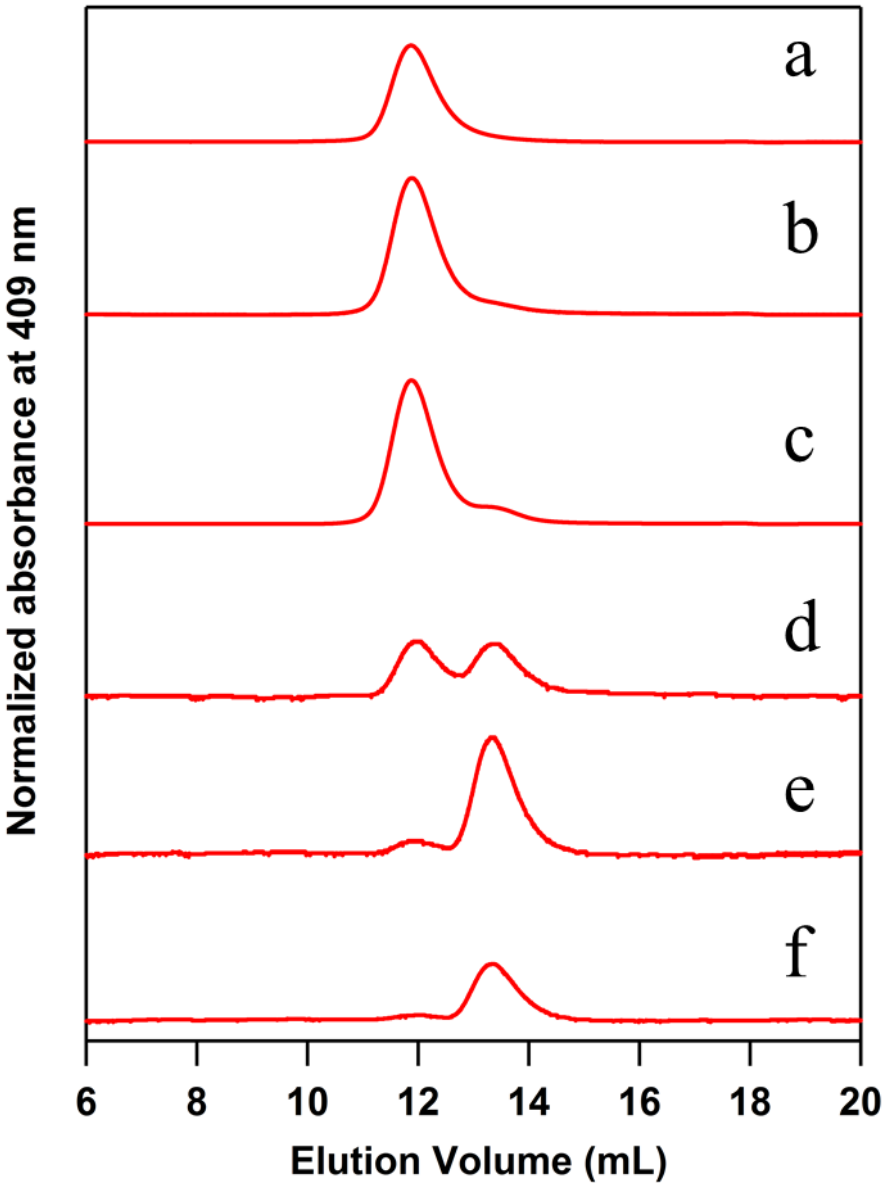

Figure 2.5 Size exclusion chromatograms of HT wild-type–M59A cyt c_{552} heterodimer with and without incubation: (a) Without incubation; (b) after incubation at 70 °C for 30 min; (c) after incubation at 75 °C for 30 min; (d) after incubation at 80 °C for 30 min; (e) after incubation at 85 °C for 30 min; (f) after incubation at 90 °C for 30 min. Measurement conditions: column, Superdex 75 10/300 GL; flow rate, 0.5 mL/min; monitoring wavelength, 409 nm; solvent, 50 mM potassium phosphate buffer (pH 7.0); temperature, 4 °C.

To obtain information on the active site and secondary structures, I performed optical absorption and CD measurements. The Soret band of oxidized HT wild-type–M59A cyt c_{552} heterodimer was observed at 402.5 nm (Figure 2.6a, blue). The absorption coefficient of the Soret band for the heterodimer was calculated as 236,000 ± 1500 $M^{-1}cm^{-1}$. The absorption coefficient value of HT wild-type cyt c_{552} monomer was reported as ε = 109,000 ± 2000 $M^{-1}cm^{-1}$ (*4*) at 409 nm, and that of HT M59A cyt c_{552} monomer was obtained as ε = 160,000 ± 1000 $M^{-1}cm^{-1}$ at 401 nm. The absorption spectrum of the heterodimer was similar to that of the sum spectrum of the absorption spectra of HT wild-type and M59A cyt c_{552} (Figure 2.6a). These results show that the active sites of the heterodimer correspond to the active sites of wild-type cyt c_{552} and M59A cyt c_{552}. The CD spectra (Figure 2.6b) were also similar between the heterodimer and the sum spectrum of the CD spectra of the monomers. These results show that the secondary structure of the heterodimer was also similar to those of the monomers.

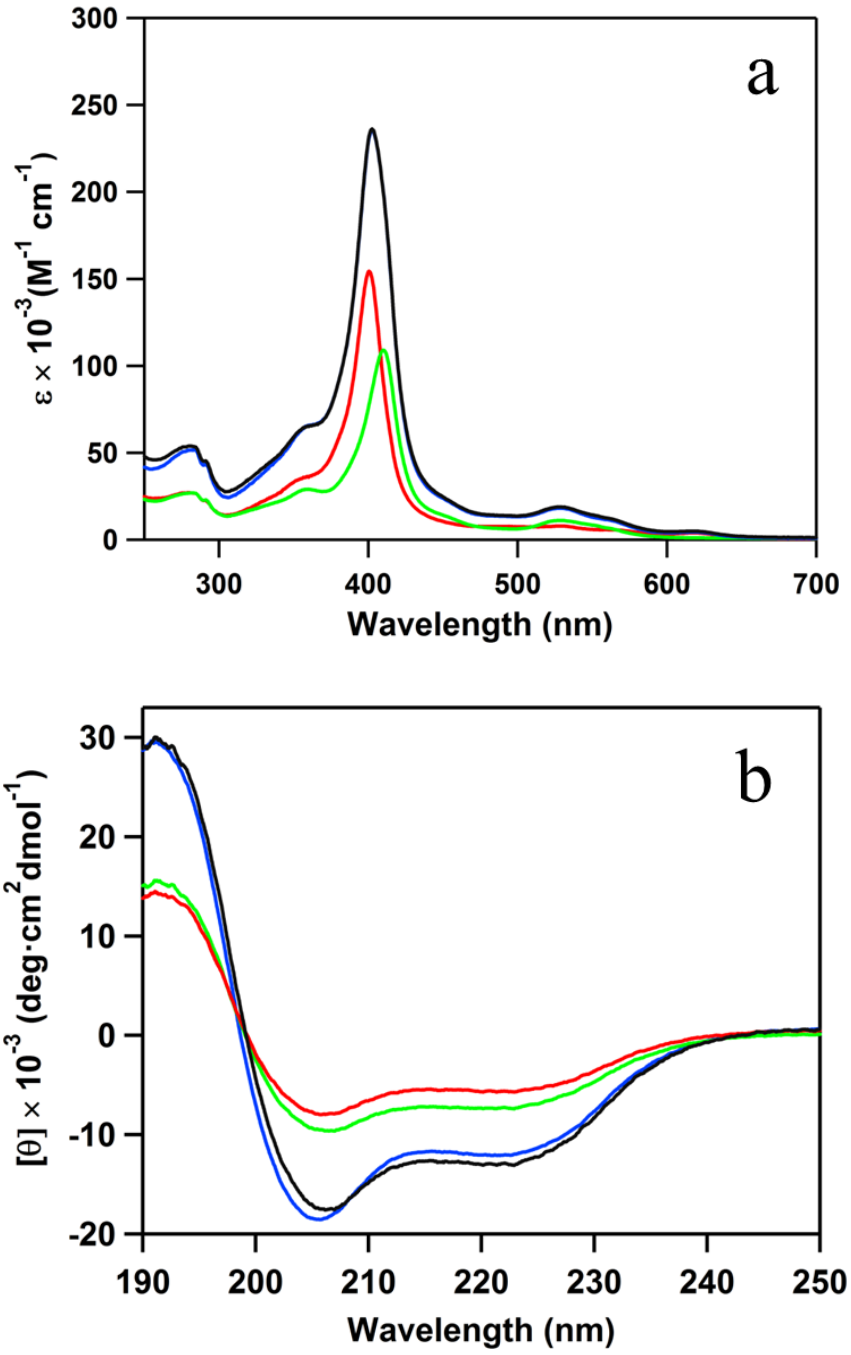

Figure 2.6 Optical absorption (a) and CD spectra (b) of the oxidized species of HT wild-type cyt c_{552} (green), HT M59A cyt c_{552} (red), heterodimer (blue), and calculated sum spectrum of HT wild-type cyt c_{552} and HT M59A cyt c_{552} (black). Measurement conditions: sample concentration, (a) 7−9 μM (heme unit) and (b) 5 μM (protein); solvent, 50 mM potassium phosphate buffer (pH 7.0); temperature, (a) room temperature and (b) 25 °C.

To obtain detailed structural information of the heterodimer, I performed crystallization of the heterodimer. I obtained high quality crystals (Figure 2.7).

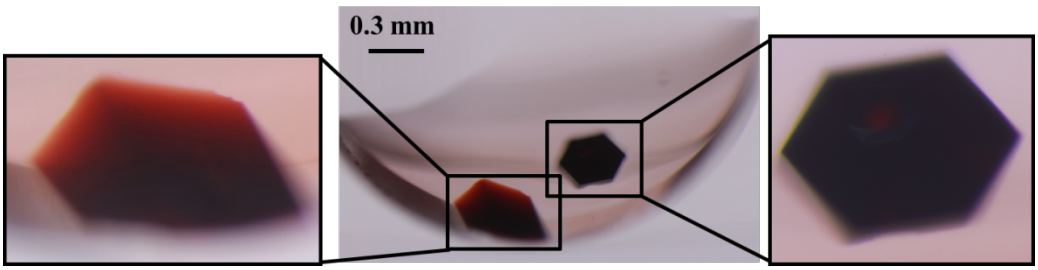

Figure 2.7 Crystals picture of HT wild-type–M59A cyt c_{552} heterodimer

The structure of heterodimer at 1.8 Å resolution exhibited a domain-swapped structure. The swapped domain contained the N-terminal α–helix and heme (Figure 2.8). However, each active site of the heterodimer showed an electron density of an average of His–Fe–Met and His–Fe–H_2O coordinations (Figure 2.9). It was difficult to distinguish the two different coordination structures in the heterodimer.

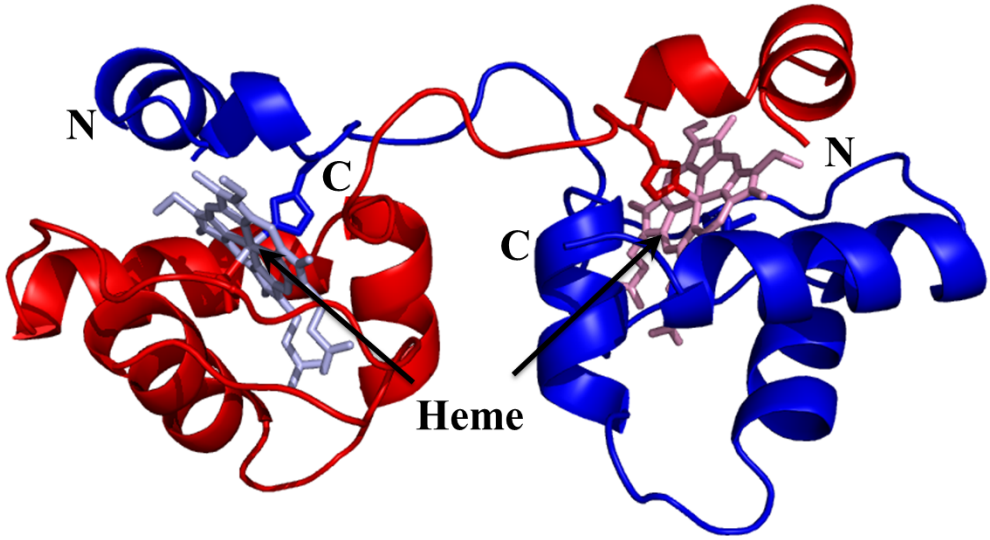

Figure 2.8 Crystal structure of HT wild-type–M59A cyt c_{552} heterodimer. The hemes are shown as stick models. Each protomer is shown in blue or red. Side-chain atoms of His14 and Met59 are shown as stick models.

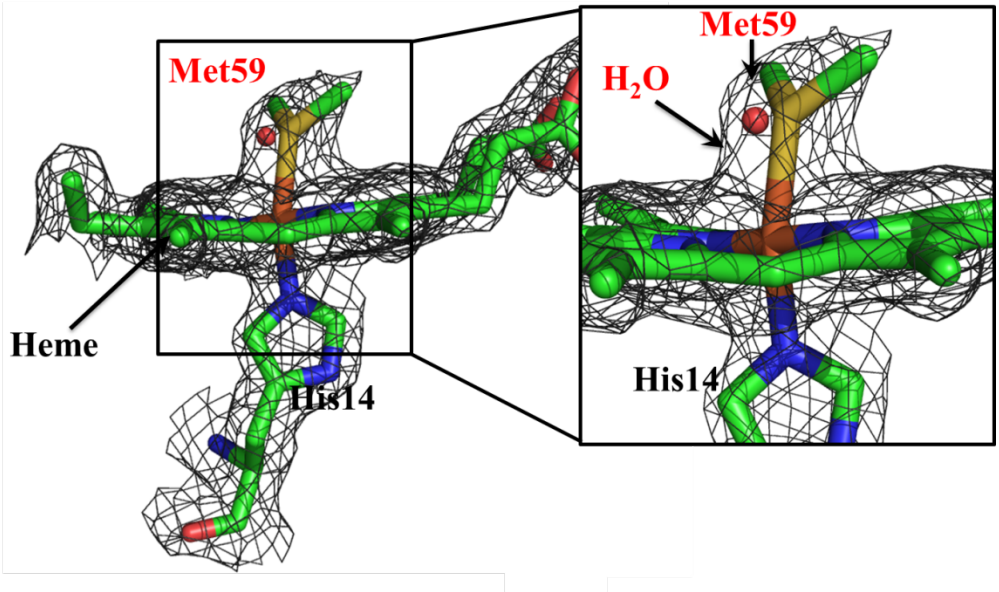

Figure 2.9 2*Fo* – *Fc* electron density map of the active site of HT wild-type–M59A cyt c_{552} heterodimer. The map is shown as mesh and contoured at 1 σ. The hemes are shown as stick models. Atoms of His14 and Met59 are shown as stick models. The heme-coordinating water molecule is shown as red sphere.

The overlapped view of the heterodimer with the wild-type monomer is showed in Figure 2.10. The protein structure of the heterodimer corresponded well to that of the wild-type monomer. The root-mean-square deviation (rmsd) values of the Cα atoms were calculated between the structures of the heterodimer and the wild-type monomer. The rmsd value was obtained as 0.31–0.42 Å (four molecules in the asymmetric unit for HT cyt c_{552} monomer) (Table 2.3). These values indicate that the structures were similar between each unit of the heterodimer and the wild-type monomer.

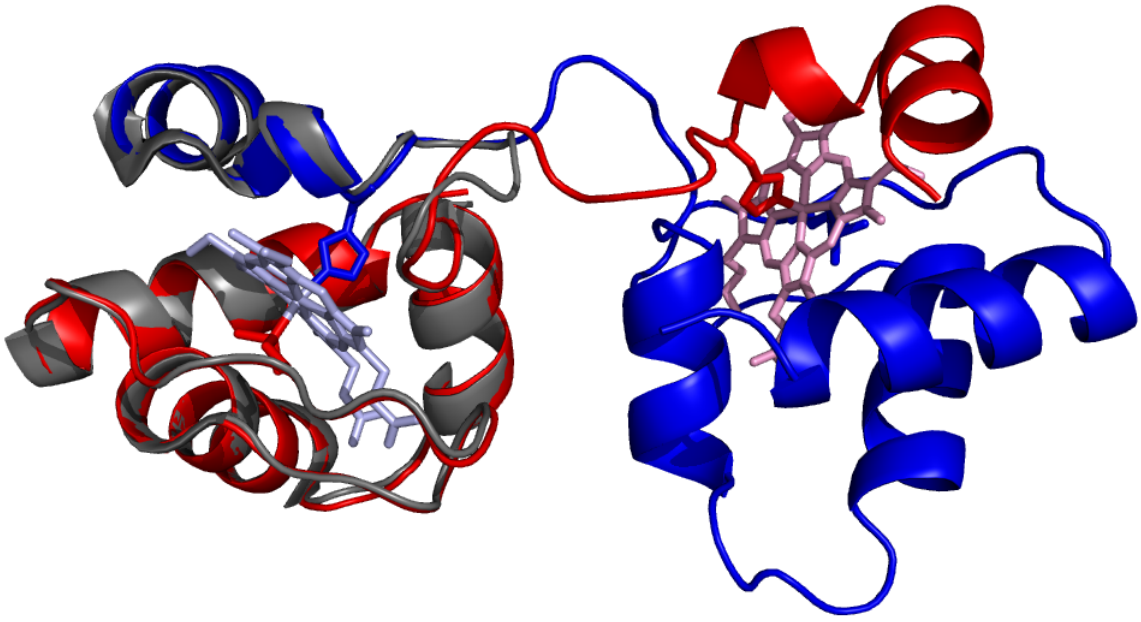

Figure 2.10 Overlapped view of the structures of the heterodimer (red and blue) and HT wild-type cyt c_{552} monomer (PDB ID: 1YNR) (gray). Side-chain atoms of His14, Met59, and the hemes are shown as stick models.

Table 2.3 Rmsd values of the Cα atoms between the cyt c_{552} heterodimer and HT wild-type cyt c_{552} monomer.[a]

	Rmsd (Å)
HT wild-type–M59A cyt c_{552} heterodimer[b]	0.31–0.42

[a]There are four independent molecules in the asymmetric unit of the monomeric HT wild-type cyt c_{552} crystal, whereas there are two protomers in the asymmetric unit of the heterodimer.
[b]Residues 1−17 of one protomer and residues 22−80 in the other protomer in the dimer were compared with the corresponding structural region of the monomer. The hinge loop (Ala18−Lys21) was excluded from the calculation.

To investigate the effect of domain-swapping on the function of the heterodimer, cyclic voltammetry was performed to obtain the redox potentials of the heterodimer and monomers (Figure 2.11). The midpoint redox potentials of HT wild-type cyt c_{552} and HT M59A cyt c_{552} monomers were obtained as 230 ± 3 mV and -94 ± 5 mV (vs NHE) in 50 mM potassium phosphate, pH 7.0, in the presence of 200 mM NaCl at room temperature. The redox potential values of the monomers were similar to the reported values (*4, 10-12*). The redox potentials of the heterodimer were obtained as 184 ± 4 mV and -208 ± 5 mV. The 184 ± 4 mV peak may correspond to the His/Met-coordinated site, whereas the peak at -208 ± 5 mV may correspond to the His/H_2O-coordinated site.

The redox potential of each peak of the heterodimer decreased 46 mV for His/Met-coordinated site and 114 mV for the His/H_2O-coordinated site. Higher solvent

accessibility stabilized the ferric form of heme proteins. The structure of heterodimer was slightly changed by domain-swapping, especially around the hinge loop. These structural changes may cause the change of solvent accessibility of the heme active site, contributing to the decrease in the redox potentials of the domain-swapped heterodimer compared to those of the monomers.

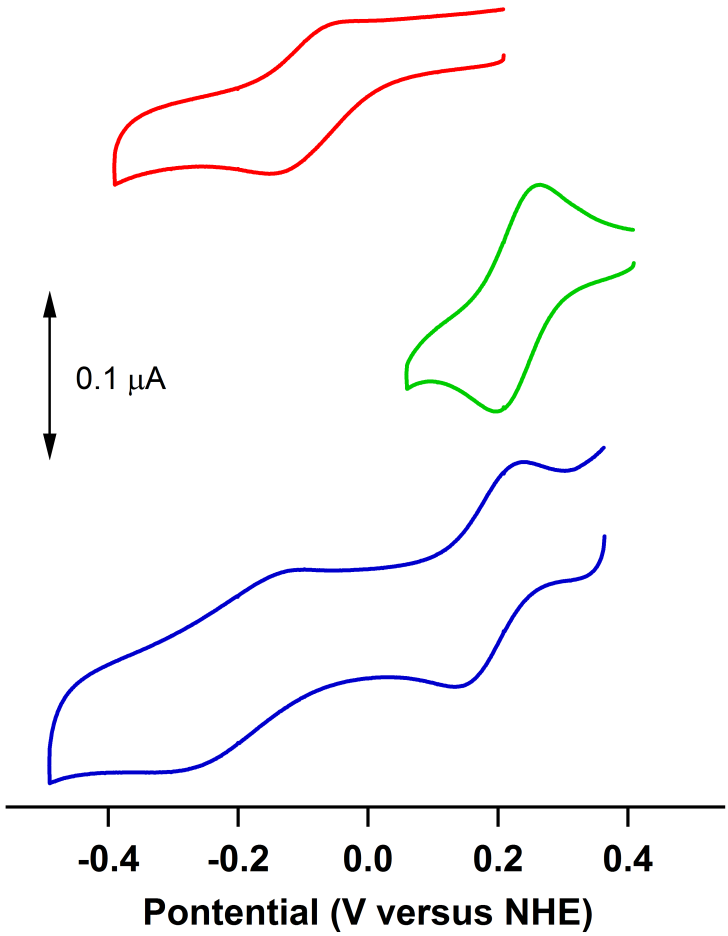

Figure 2.11 Cyclic voltammograms of HT M59A cyt c_{552} monomer (red), HT wild-type cyt c_{552} monomer (green) and the heterodimer (blue). Scan rate, 20 mV/s; buffer, 50 mM potassium phosphate buffer (pH 7.0), containing 200 mM NaCl.

2-1-4 Conclusion

Heterodimer consisted of HT wild-type and M59A cyt c_{552} has been constructed by exchanging the N-terminal region containing the heme. The heterodimer contained two different active sites, His–Fe–Met and His–Fe–H_2O. These results demonstrate that domain-swapping can be utilized to design multi-heme proteins with different active sites.

Section 2-2

Construction of heterodimer with different active sites using chimeric proteins PA*c*-HT*c* M61A and HT*c*-PA*c*

2-2-1 Introduction

Since it was difficult to distinguish two different coordination sites of the cyt c_{552} heterodimer, a new heterodimer was constructed using chimeric proteins base on domain-swapping. Domain-swapped HT cyt c_{552} dimer and PA cyt c_{551} dimer have been reported, which exhibited similar swapping region, N-terminal region containing the heme (*4, 13*). The heme active sites were similar between dimeric PA cyt c_{551} and HT cyt c_{552}, where Met and His were coordinated to the heme iron. In this study, PA cyt c_{551} and HT cyt c_{552} were used to construct chimeric proteins. We exchanged the N-terminal and C-terminal domains of PA cyt c_{551} and HT cyt c_{552} between each other to obtain two chimeric proteins, PA*c*-HT*c* and HT*c*-PA*c* (Figure 2.12). Met was replaced with Ala in the PA*c*-HT*c* chimeric protein, and a heterodimer was constructed by domain-swapping PA*c*-HT*c* M61A and HT*c*-PA*c*. This heterodimer would contain different active sites.

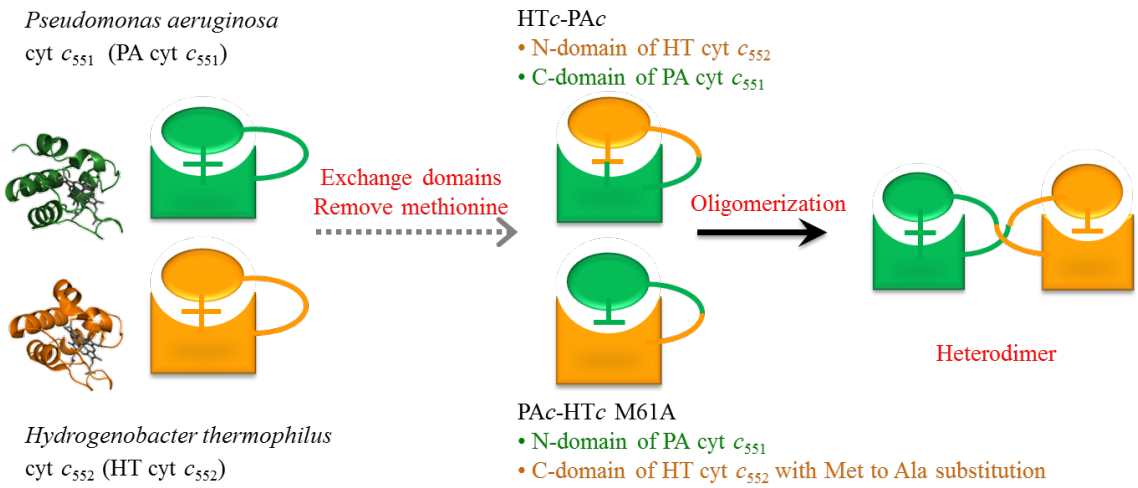

Figure 2.12 Design strategy for construction of the heterodimer of PA*c*-HT*c* M61A and HT*c*-PA*c*

2-2-2 Materials and methods

2-2-2-1 Plasmids for PA*c*-HT*c* M61A and HT*c*-PA*c*

Synthesized DNAs encoding PA*c*-HT*c* and HT*c*-PA*c* (Eurofins genonics) were treated with restriction enzyme, *Eco*RI and *Sal*I. The resulting DNA fragments were ligated to pKK223-3 expression plasmid treated with *Eco*RI and *Sal*I. Met61 of PA*c*-HT*c* was substituted with Ala (PA*c*-HT*c* M61A). Point mutation of Met to Ala was introduced by PCR-based *in vitro* mutagenesis using forward and reverse primers (Euro fins genomics) (Table 2.4), and Primer STAR max DNA polymerase (Takara Bio). Plasmid DNAs were prepared using *E. coli* DH5α cells, and purified with QIAprep spin Mini prep kit (Qiagen). DNA sequencing was conducted with the BigDye Terminator version 3.1 cycle sequencing kit (Applied Biosystems, Inc., Foster City, CA) and an ABI PRISM 3100 genetic analyzer sequencing system (Applied Biosystems, Inc.). The constructed plasmids were introduced into *E. coli* JCB387 cells containing the PEC86 plasmid DNA.

2-2-2-2 Purification of chimeric proteins PA*c*-HT*c* M61A and HT*c*-PA*c*

PA*c*-HT*c* M61A and HT*c*-PA*c* were overproduced in *E. coli* JCB387 cells. The *E. coli* cells were grown aerobically in 25 g/L LB broth at 37 °C until OD_{600} reached

around 1.5, then harvested by centrifugation (8,000 g, 5 min, 4 °C). After centrifugation, the cells were suspended in spheroplasting buffer (100 mM Tris-HCl buffer, pH 8.0, containing 10 mM EDTA and 20 % (w/v) sucrose) to extract periplasmic protein by the osmotic method. Suspended cells were incubated on ice for 30 min, and then centrifuged (13,700 g, 30 min, 4 °C), the resulting supernatant was collected. The cells were suspended again in pure water and incubated on ice for 30 min. After centrifugation (13,700 g, 30 min, 4 °C), the supernatant was collected and added to the supernatant obtained in the previous step. The protein solution was dialyzed overnight at 4 °C with 25 mM sodium acetate buffer, pH 5.0. The proteins were oxidized by an addition of excess (~10 fold) potassium ferricyanide. Protein solution was purified by cation exchange chromatography (CM-cellulose column (Wako), HiTrap SP column (GE healthcare)) with a gradient of 0 to 300 mM Na_2SO_4. Subsequently, proteins were purified by size exclusion chromatography (HiLoad 26/60 Superdex 75, GE healthcare) using a FPLC system (BioLogic DuoFlow 10, Bio-Rad, CA) at 4 °C, with 50 mM potassium phosphate buffer, pH 7.0.

Molar extinction coefficients of chimeric proteins were obtained with the pyridine hemochrome method (ε = 147, 500 ± 2000 $M^{-1}cm^{-1}$ at 401 nm for the PA*c*-HT*c* M61A mutant; ε = 116,800 ± 3000 $M^{-1}cm^{-1}$ at 409 nm for the HT*c*-PA*c*) (*3*).

The concentrations of the chimeric proteins were calculated from the absorbance at 401 nm and 409 nm with the absorption coefficients.

2-2-2-3 Oligomerization of HT*c*-PA*c* and PA*c*-HT*c* M61A heterodimer

HT*c*-PA*c* and PA*c*-HT*c* M61A were mixed with 1:1 molar ratio in 50 mM potassium phosphate buffer, pH 7.0. Ethanol was added to the mixture solution at 50 °C as a final concentration of 80 % (v/v). The resulting precipitate was separated from the supernatant by centrifugation at 10,000 g for 10 min. The obtained precipitate was lyophilized to remove the residual ethanol and then dissolved with 2 mL of 50 mM potassium phosphate buffer, pH 7.0, at 4 °C. The Oligomer formation was analyzed by size exclusion chromatography (HiLoad 26/60 Superdex 75, GE healthcare) with the FPLC system (BioLogic DuoFlow 10, Bio-Rad, CA) at a flow rate of 1.0 mL/min at 4 °C. Fraction containing dimers was collected and the buffer was changed to 25 mM sodium acetate buffer, pH 5.0. The dimers were further purified by cation exchange chromatography (Mono S^{TM} 5/50 GL column, GE healthcare) using the FPLC system with 25 mM sodium acetate buffer, pH 5.0, at a flow rate of 0.5 mL/min at 4 °C. The fractions containing the dimers were eluted with a gradient of 25 to 125 mM Na_2SO_4 over a period of 200 min. The cation exchange chromatography (Mono S^{TM} 5/50 GL

column) was performed again to purify heterodimer.

The molar extinction coefficient of the heterodimer was obtained by pyridine hemechrome method (253,400 ± 2000 $M^{-1}cm^{-1}$ at 402 nm) (*2*). The concentration of the heterodimer was calculated from the absorbance at 402 nm.

2-2-2-4 MALDI-TOF mass measurement

The buffer of protein solutions was changed to pure water by ultra filtration using Amicon Ultra (MWCO 3000, Millipore). MALDI-TOF mass spectrum of heterodimer was obtained with an Autoflex II mass spectrometer (Bruker Daltonics) in linear mode using sinapinic acid as a matrix.

2-2-2-5 Optical absorption spectra and CD measurements

UV-2450 spectrophotometer (Shimadzu, Japan) and J-725 CD spectropolarimeter (Jasco, Japan) were used for optical absorption and CD measurements, respectively. 1-cm-path-length and 0.1-cm-path-length quartz cells were used for optical absorption and CD measurements, respectively.

2-2-2-6 Stability measurement of heterodimer

The stability of the heterodimer was measured by the incubation of the heterodimer solution for 30 min at various temperatures (50 to 75 °C), and then analyzed by size exclusion chromatography (Superdex 75 10/300 GL, GE helthcare) using the FPLC system (BioLogic DuoFlow 10, Bio-Rad, CA) equilibrated with 50 mM potassium phosphate buffer, pH 7.0, at a flow rate of 0.5 mL/min at 4 °C.

2-2-2-7 Reduction potential measurement

Redox potentials were measured as described above (section 2-1-2-7)

2-2-2-8 X-ray crystallographic analysis

Crystals of HT*c*-PA*c* and PA*c*-HT*c* M61A heterodimer was obtained by the sitting drop vapor diffusion method with crystal plates (CrystalClear D Strips, Douglas Instruments, Hampton Research, CA). Oxidized heterodimer was dissolved in 10 mM HEPES buffer, pH 7.0. The protein concentration of the heterodimer was 14.2 mg/mL. Droplets were prepared by mixing 1 μL of the heterodimer solution with 1 μL reservoir solution and were equilibrated. The best reservoir solution was found to be 100 mM MES, pH 6.5, containing 25 % (w/v) PEG 6,000 for heterodimer. A crystal was observed after incubation at 4 °C for one month.

The diffraction data were collected at the BL26B1 beamline of SPring-8 (Japan) for heterodimer using a EIGER4M (Dectris). The crystal was mounted on a cryo-loop and flash-frozen at 100 K in a nitrogen cryo system. The crystal-to-detector distance was 125 mm, and the wavelength was 1.0000 Å. The oscillation angle was 1.0°, and the exposure time was 5 s per frame. The total number of frames was 180. The diffraction data were processed using the program HKL2000 for heterodimers.

The preliminary structure was obtained by a molecular replacement programs using the atomic coordinates of the structures of monomeric HT wild-type cyt c_{552} (PDB code: 1YNR) and PA wild-type cyt c_{551} (PDB code: 351C) as a starting models for the heterodimer.

The structure refinement was performed using the program, REFMAC (*7, 8*). The molecular model was manually corrected, and water molecules were picked up in the electron density map using the program, COOT (*9*). The data collection and refinement statistics of the heterodimer is summarized in Table 2.5.

Table 2.4 Nucleotide sequences of primers.

Primer	Sequence[a]
PA*c*-HT*c*/M61A-fw	GTTCCCGCACCTCCTCAAAATGTAACCGATG
PA*c*-HT*c*/M61A-rv	AGGAGGTGCGGGAACAGAACCCCACAC

[a]Underlines indicate the nucleotides for the modified amino acid.

Table 2.5 Statistics of data collection and structure refinement for HT*c*-PA*c* and PA*c*-HT*c* M61A heterodimer.

Data collection			
X-ray source	SPring-8 (BL26B1)		
Wavelength (Å)	1.0000		
Space group	$P2_1$		
Unit cell parameters			
a, *b*, *c* (Å)	32.1	65.9	35.4
α, β, γ (º)	90.0	103.7	90.0
Resolution (Å)	50.0–1.55 (1.58–1.55)		
Number of unique reflections	21840 (1164)		
R_{merge}[a]	0.044 (0.533)		
Completeness (%)	99.5 (96.3)		
$\langle I/\sigma(I)\rangle$	26.6 (2.0)		
$CC_{1/2}$	0.998 (0.755)		
Redundancy	3.3 (3.1)		
Refinement			
Resolution (Å)	34.4–1.55 (1.59–1.55)		
Number of reflections	19118 (1134)		
R_{work}[b]	0.2087 (0.266)		
R_{free}[b]	0.2376 (0.279)		
Completeness (%)	96.6 (73.6)		
Number of atoms in an asymmetric unit			
Protein	1208		
Water	67		
Heme	86		
Average *B* factors (Å^2)			
Protein	19.3		
Water	19.2		
Heme	9.6		
Ramachandran plot (%)			
Favored	100.0		
Allowed	0		
Outlier	0		

Statistics for the highest-resolution shell are given in parentheses.
[a] $R_{merge}=\Sigma_{hkl} | I- \langle I\rangle | (\Sigma_{hkl}| I |)^{-1}$.
[b] $R_{work}=\Sigma_{hkl} | | F_{obs} | - k| F_{calc} | | (\Sigma_{hkl} | F_{obs} |)^{-1}$, k: scaling factor. R_{free} was computed identically, except where all reflections belong to a test set of 5 % of randomly selected data.

2-2-3 Results and discussion

Oligomers formed by an addition of 80 % (v/v) ethanol at 50 °C to a mixture of chimeric proteins. The peak correspond to the dimer was obtained in the size exclusion chromatogram. The dimeric cyt *c* was purified by cation exchange chromatography (Figure 2.14). The observation of several peaks in Mono S chromatogram indicate that the dimer fraction includes several dimer forms, i.e., the heterodimer and homodimers. Each peak in the chromatogram was analyzed by MALDI-TOF mass spectrometry. The MALDI-TOF mass spectrum of the fraction 72–78 mL is shown in Figure 2.15. The spectrum showed two peaks at m/z 9110 and m/z 9328. These peaks at m/z 9110 and m/z 9328 corresponded well to theoretical molecular weights of positively charged chimeric HT*c*-PA*c* and PA*c*-HT*c* M61A, m/z 9111 and m/z 9329, respectively. These results indicate that HT*c*-PA*c* and PA*c*-HT*c* M61A constructed the dimer.

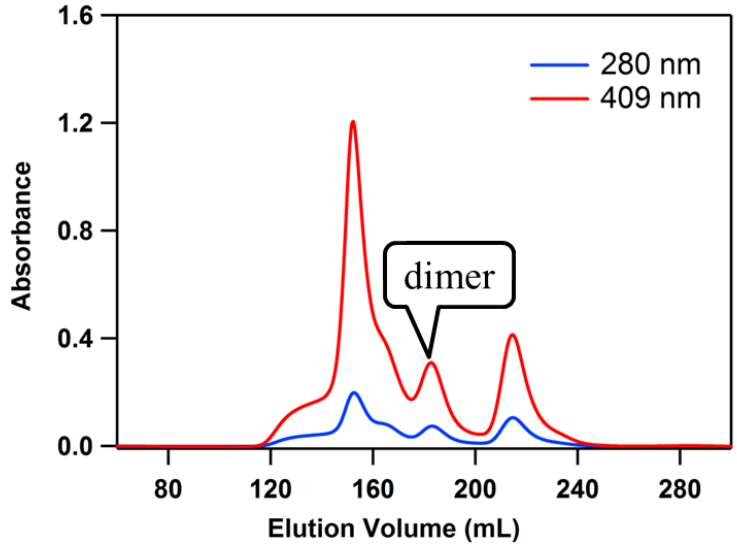

Figure 2.13 Size exclusion chromatogram of HT*c*-PA*c* and PA*c*-HT*c* M61A oligomer. Measurement conditions: column, HiLoad 26/60 Superdex 75; flow rate, 1.0 mL/min; monitoring wavelength, 280 nm (blue) and 409 nm (red); solvent, 50 mM potassium phosphate buffer (pH 7.0); temperature, 4 °C.

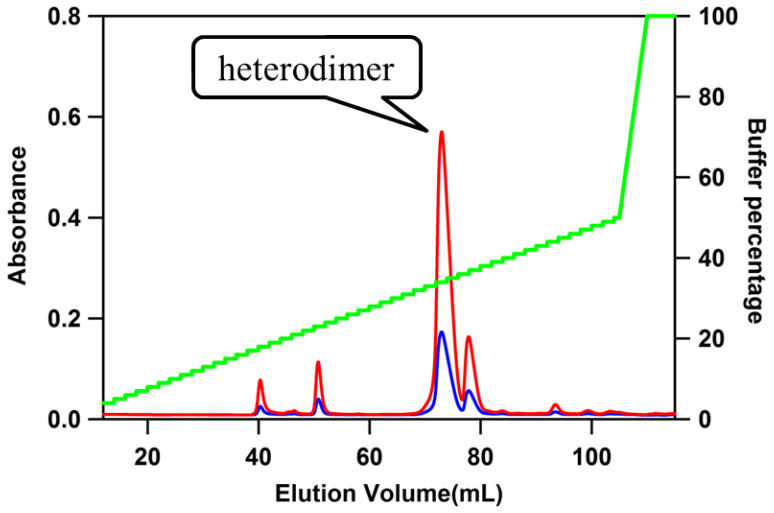

Figure 2.14 Cation exchange chromatogram of HT*c*-PA*c* and PA*c*-HT*c* M61A dimers. Measurement conditions: column, Mono S^{TM} 5/50 GL column; flow rate, 0.5 mL/min; monitoring wavelength, 280 nm (blue), and 409 nm (red); solvent, buffer A: 25 mM sodium acetate buffer (pH 5.0), and buffer B: 25 mM sodium acetate buffer (pH 5.0), containing 250 mM Na_2SO_4; gradient 10–50 % of B buffer over a period of 200 min (green); temperature, 4 °C.

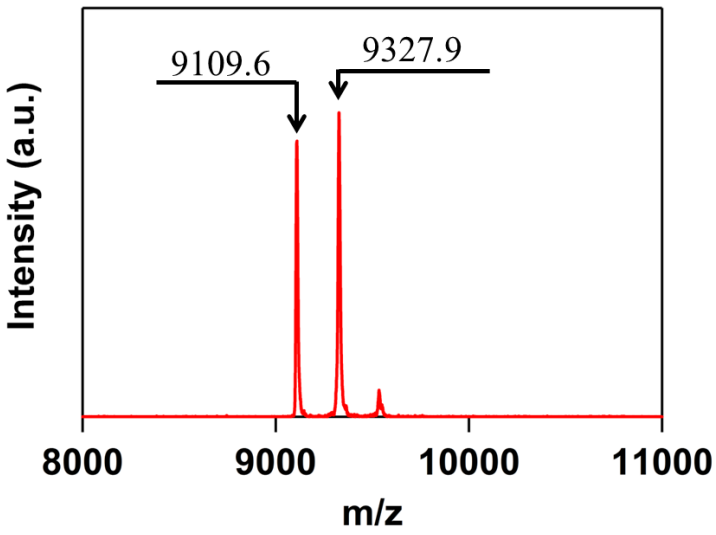

Figure 2.15 MALDI-TOF mass spectrum of the purified heterodimer. Measurement conditions: solvent, pure water; matrix, sinapinic acid.

To investigate the stability, the HT*c*-PA*c* and PA*c*-HT*c* M61A heterodimer was incubated for 30 min at various temperatures between 50 to 75 °C (Figure 2.16). The heterodimer dissociated to monomers by the incubation higher than 60 °C, but not at temperatures lower than 50 °C.

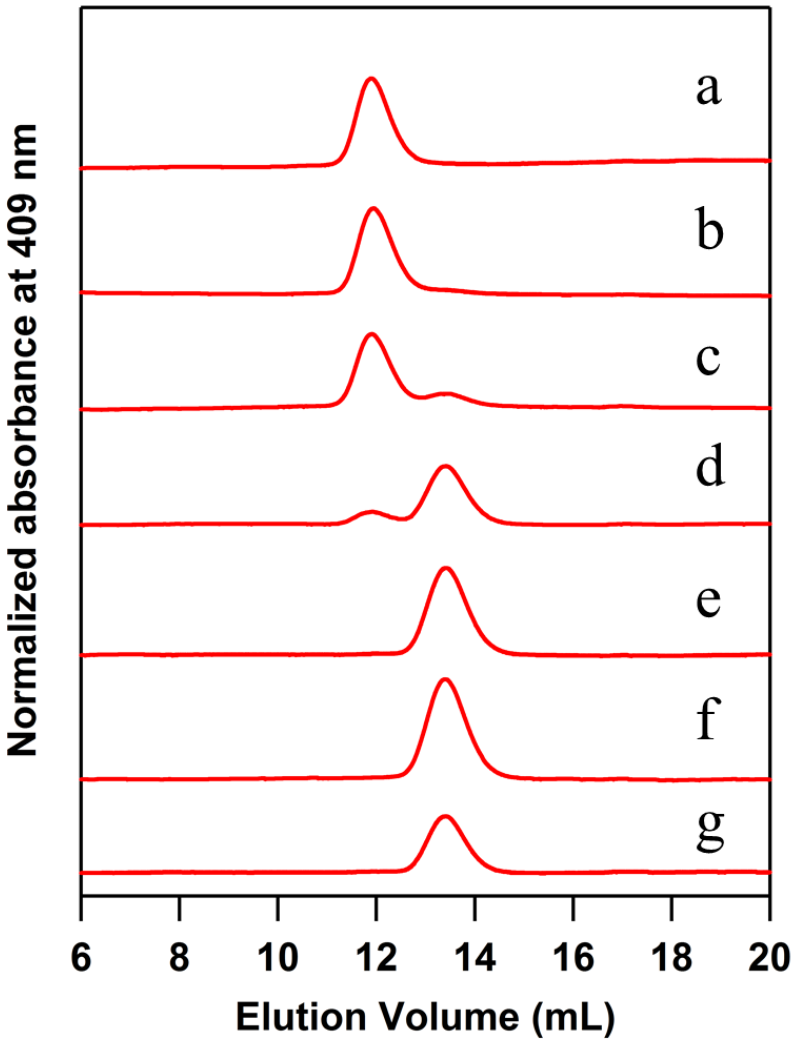

Figure 2.16 Size exclusion chromatograms of HT*c*-PA*c* and PA*c*-HT*c* M61A heterodimer with and without incubation: (a) Without incubation; (b) after incubation at 50 °C for 30 min; (c) after incubation at 55 °C for 30 min; (d) after incubation at 60 °C for 30 min; (e) after incubation at 65 °C for 30 min; (f) after incubation at 70 °C for 30 min; (g) after incubation at 75 °C for 30 min. Measurement conditions: column, Superdex 75 10/300 GL; flow rate, 0.5 mL/min; monitoring wavelength, 409 nm; solvent, 50 mM potassium phosphate buffer (pH 7.0); temperature, 4 °C.

To obtain information on the active site and secondary structures, I performed optical absorption and CD measurements. The Soret band of oxidized HT*c*-PA*c* and

PA*c*-HT*c* M61A heterodimer was observed at 402 nm (Figure 2.17a, blue). The absorption coefficient of the Soret band for the heterodimer was calculated as 253,400 ± 2000 $M^{-1}cm^{-1}$. The absorption coefficient value of PA wild-type cyt c_{551} monomer was reported as ε = 106,100 $M^{-1}cm^{-1}$ at 409 nm (*14*), and that of HT M59A cyt c_{552} monomer was obtained as ε = 160,000 ± 1000 $M^{-1}cm^{-1}$ at 401 nm in this study. The absorption spectrum of the heterodimer was similar to that of the sum spectrum of the absorption spectra of PA wild-type cyt c_{551} and HT M59A cyt c_{552} (Figure 2.17a). The CD spectra were also similar between the heterodimer and the sum spectrum of the CD spectra of the monomers. These results show that the active site and secondary structures of the heterodimer were similar to those of the monomers.

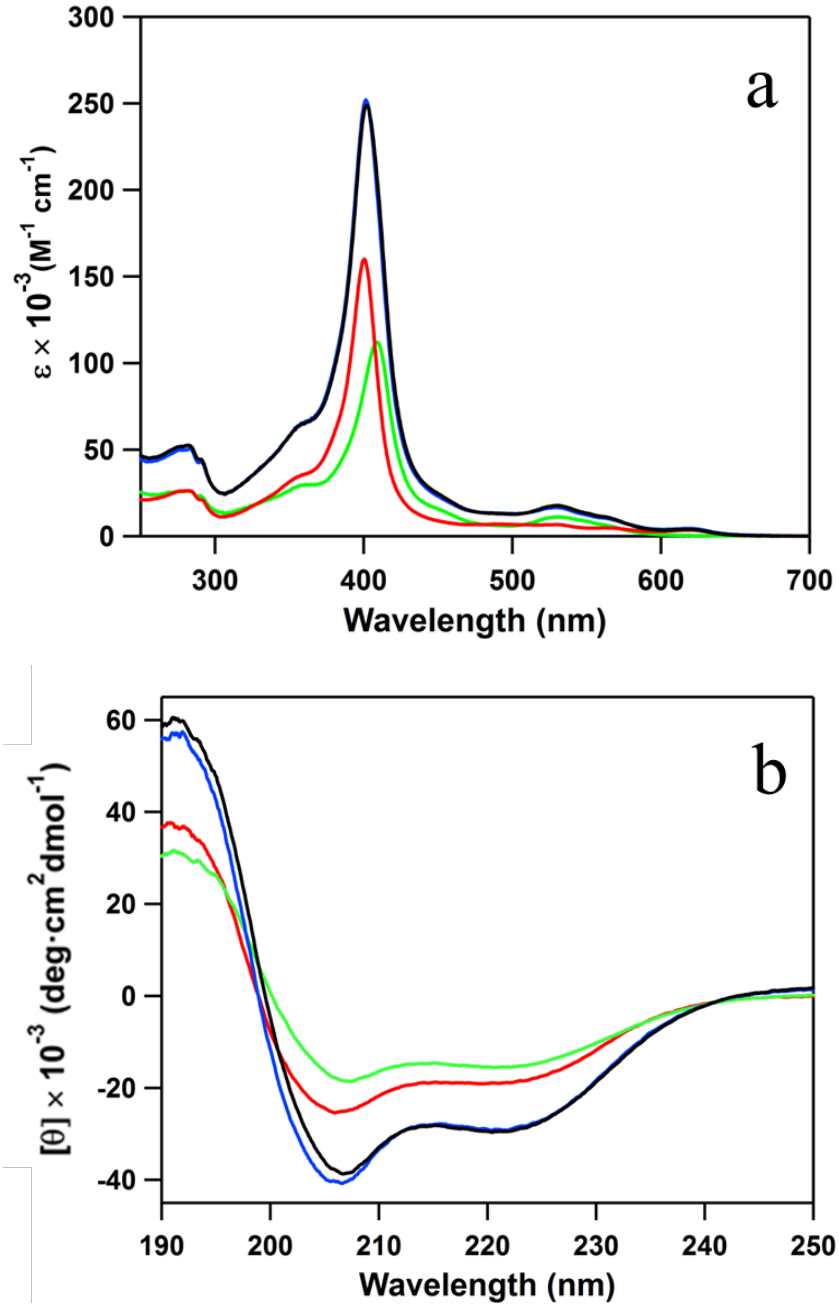

Figure 2.17 Optical absorption (a) and CD spectra (b) of the oxidized HT*c*-PA*c* and PA*c*-HT*c* M61A heterodimer (blue), calculated sum spectrum of PA wild-type cyt c_{551} and HT M59A cyt c_{552} (black), HT M59A cyt c_{552} (red) and PA cyt c_{551} (green). Measurement conditions: sample concentration (heme), (a) 7–9 μM and (b) 10 μM; solvent, 50 mM potassium phosphate buffer (pH 7.0); temperature, (a) room temperature and (b) 25 °C.

To obtain detailed structural information of the heterodimer, I performed crystallization of the heterodimer. I obtained high quality crystals (Figure 2.18).

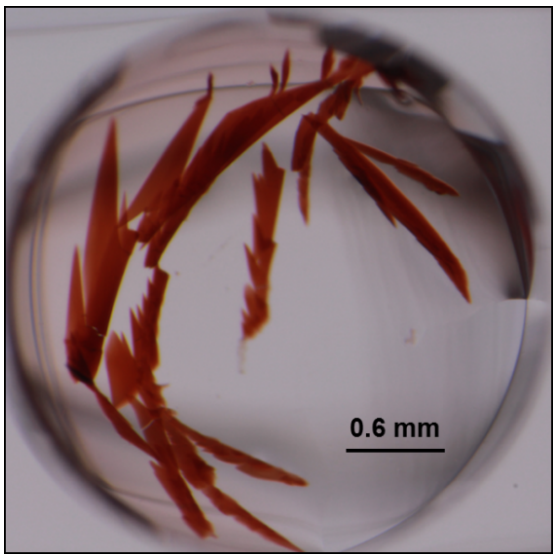

Figure 2.18 Crystals picture of HT*c*-PA*c* and PA*c*-HT*c* M61A heterodimer.

The structure of HT*c*-PA*c* and PA*c*-HT*c* M61A heterodimer at 1.55 Å resolution exhibited a domain-swapped structure (Figure 2.19). The swapped domain contained the N-terminal α–helix and heme. The heterodimer contained two different active sites.

The overlapped view of the HT*c*-PA*c* and PA*c*-HT*c* M61A heterodimer with the PA cyt c_{551} and HT cyt c_{552} wild-type monomers is shown in Figure 2.20. The protein structure of the heterodimer corresponded well to those of the wild-type monomers. The rmsd values of the Cα atoms were calculated between the heterodimer and the wild-type monomers. The rmsd values were obtained as 0.50 Å for PA part of heterodimer and

0.27–0.42 Å for HT M59A part of heterodimer (four molecules in the asymmetric unit for HT cyt c_{552} monomer) (Table 2.6). These values indicate that the structures were similar between each unit of the heterodimer and the wild-type monomers.

In the active site structures of the PA cyt c_{551} part of the heterodimer, His and Met coordinated to the heme as in the PA wild-type cyt c_{551} (Figure 2.21). Due to replacement of Met with Ala in PA*c*-HT*c* M61A, a water molecule coordinated to the heme of HT*c*-PA*c* in the HT M59A cyt c_{552} part of the heterodimer.

The Fe–His14 distances of the heterodimer were 2.04 and 2.02 Å (PA cyt c_{551} part of heterodimer: 2.04 Å; HT M59A cyt c_{552} part of heterodimer: 2.02 Å), whereas the Fe–Met61 and Fe–OH_2 distances were 2.29 Å and 2.00 Å, respectively. These distances were similar to the corresponding distances in the HT cyt c_{552} and PA cyt c_{551} monomers (HT cyt c_{552} monomer: Fe–His14, 2.05–2.09 Å; Fe–Met59, 2.33–2.40 Å; PA cyt c_{551} monomer: Fe–His16, 1.99 Å; Fe–Met61, 2.36 Å) (Table 2.7), although the ligands are different between HT wild-type cyt c_{552} monomer (Met) and the HT M59A cyt c_{552} part of the heterodimer (H_2O). There are five water molecules in the heme pocket of the HT M59A cyt c_{552} part of the heterodimer. The hydrogen bonding network was created in the heme pocket of the heterodimer (Figure 2.22).

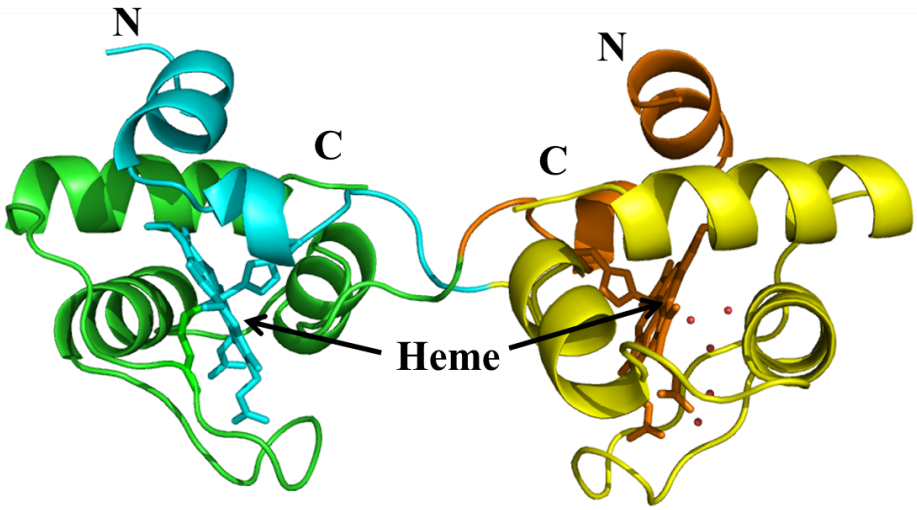

Figure 2.19 Crystal structure of HT*c*-PA*c* and PA*c*-HT*c* M61A heterodimer. Chimeric protein HT*c*-PA*c* is shown as green and orange and PA*c*-HT*c* M61A is shown as yellow and cyan. The exchanged domains are shown as cyan and orange. The hemes, side-chain atoms of His16 and Met59 of the PA cyt c_{551} part and His14 of the HT M59A cyt c_{552} part are shown as stick models. Water molecules at the heme pocket are shown as red sphere.

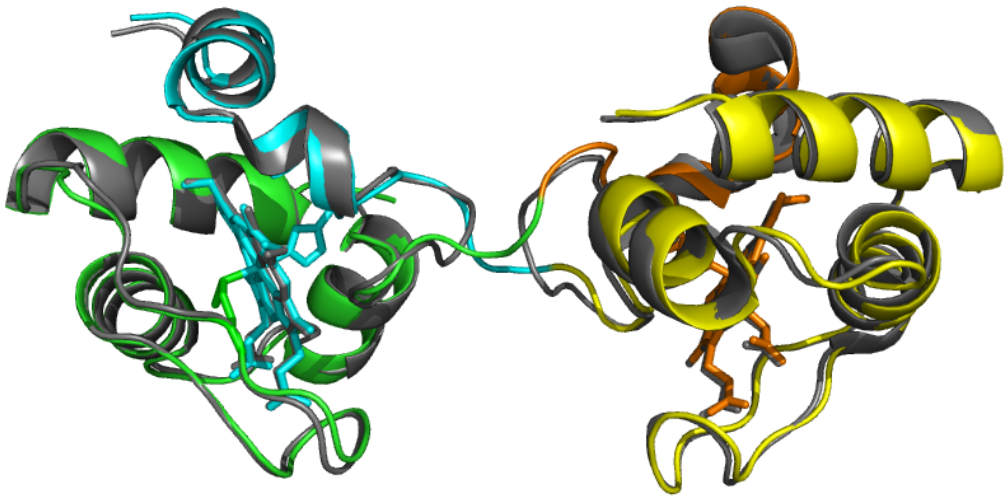

Figure 2.20 Overlapped view of the HT*c*-PA*c* and PA*c*-HT*c* M61A heterodimer (orange-green and cyan-yellow, respectively) with PA wild-type cyt c_{551} monomer (PDB ID: 351C) and HT wild-type cyt c_{552} monomer (PDB ID: 1YNR) (gray). Side-chain atoms of His14, His16, Met59, and the hemes are shown as stick models.

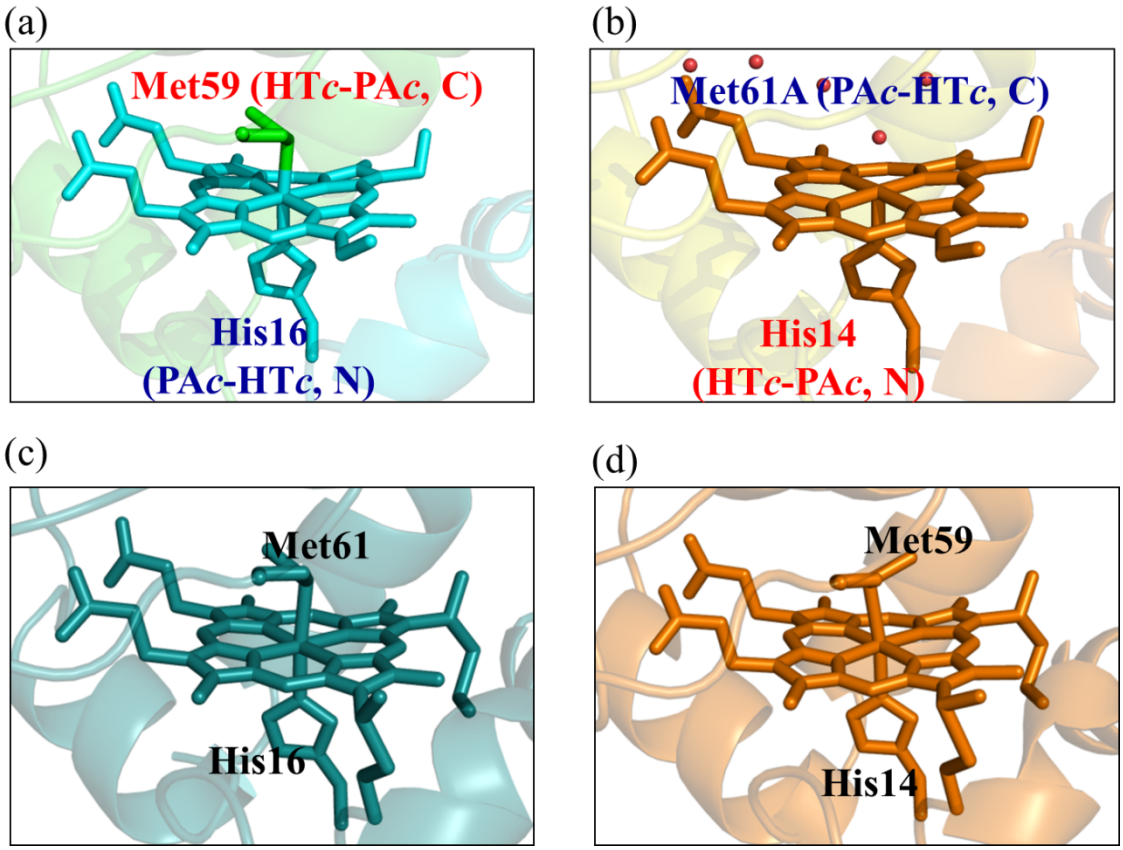

Figure 2.21 Active site structures of the heterodimer of HT*c*-PA*c* and PA*c*-HT*c* M61A (a and b), PA wild-type cyt c_{551} monomer (c) (PDB ID: 351C) and HT wild-type cyt c_{552} monomer (d) (PDB ID: 1YNR). The hemes are shown in stick models. The green, cyan regions in (a) and orange, yellow regions in (b) belonged to different protomers. Side-chain atoms of heme-coordinating His and Met are shown as stick models. Water molecules in the heme pocket are shown as red sphere in (b).

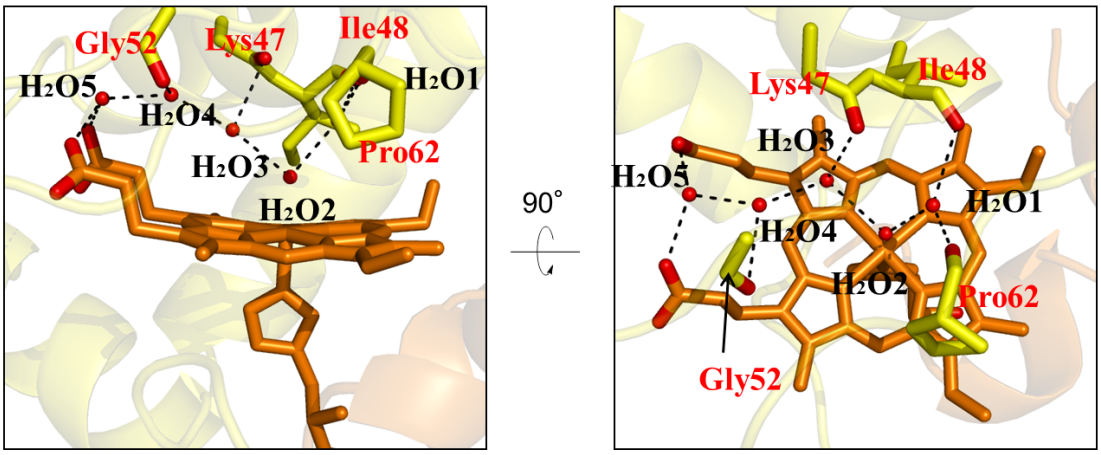

Figure 2.22 Schematic view of the hydrogen bonds in the heme pocket of the HT M59A cyt c_{552} part of the HT*c*-PA*c* and PA*c*-HT*c* M61A heterodimer. Lys47, Ile48, Gly52, and Pro62 are shown as yellow stick models. The heme is shown as an orange stick model. Hydrogen bonds between the backbone atoms are depicted in black broken lines. The oxygen atoms of the heme are depicted in red. Water molecules are shown as red sphere.

Table 2.6 Rmsd values of the Cα atoms between the protomers of the HT*c*-PA*c* and PA*c*-HT*c* M61A heterodimer and PA wild-type cyt c_{551} or HT wild-type cyt c_{552} monomer[a].

	Rmsd (Å)
PA cyt c_{551} part[b]	0.50
HT M59A cyt c_{552} part[c]	0.27–0.42

[a]There are four independent molecules in the asymmetric unit of the monomeric HT wild-type cyt c_{552} crystal, whereas there are two protomers in the asymmetric unit of the heterodimer of HT*c*-PA*c* and PA*c*-HT*c* M61A.

[b]Residues 1–18 of one PA*c*-HT*c* M61A and residues 20–80 of HT*c*-PA*c* were compared with the corresponding structural region of the monomeric PA wild-type cyt c_{551}. The hinge loop (Asp19–Met22) in PA wild-type cyt c_{551} was excluded from the calculation.

[c]Residues 1–16 of HT*c*-PA*c* and residues 23–82 of PA*c*-HT*c* M61A were compared with the corresponding structural region of the monomeric HT wild-type cyt c_{552}. The hinge loop and heme-coordinating Met (Lys17–Lys19 and Met59 in HT wild-type cyt *c*

$_{552}$) were excluded from the calculation.

Table 2.7 Fe−His and Fe−Met distances of the HT*c*-PA*c* and PA*c*-HT*c* M61A heterodimer, PA wild-type cyt c_{551} monomer, and HT wild-type cyt c_{552} monomer [a].

	Fe−His (Å)	Fe−Met (or H_2O) (Å)
PA wild-type cyt c_{551} [b]	1.99	2.36
PA cyt c_{551} part	2.04	2.29
HT wild-type cyt c_{552} [c]	2.05–2.09	2.33–2.40
HT M59A cyt c_{552} part	2.02	2.00 (H_2O)

[a]There is one dimer molecule in the asymmetric unit of the heterodimer of the HT*c*-PA*c* and PA*c*-HT*c* M61A crystal.
[b]PDB ID: 351C.
[c]PDB ID: 1YNR. There are four independent HT cyt c_{552} molecules in the asymmetric unit of the monomeric HT cyt c_{552} crystal.

To investigate the effect of domain-swapping on the function of heterodimer, cyclic voltammetry was performed to obtain the redox potentials of the heterodimer and monomers (Figure 2.23). The midpoint redox potentials of monomeric PA wild-type cyt c_{551} and HT M59A cyt c_{552} monomers were obtained as 278 ± 3 mV and -94 ± 5 mV (vs NHE) in 50 mM potassium phosphate, pH 7.0, in the presence of 200 mM NaCl at room temperature. The redox potential values of the monomers were similar to the reported values (*11-13*). The redox potentials of the heterodimer were obtained as 232 ± 4 mV and -135 ± 5 mV. The 232 ± 4 mV peak may correspond to the His–Met coordinated site, whereas the peak at -135 ± 5 mV may correspond to the His–H_2O coordinated site.

The redox potential of each peak of the heterodimer decreased 46 mV for

His/Met coordinated site and 41 mV for the His/H_2O-coordinated site. Higher solvent accessibility stabilized the ferric form of heme proteins. The structure of heterodimer was slightly changed by domain-swapping, especially around the hinge loop. These structural changes may cause the change of solvent accessibility of the heme active site, contributing to the decrease in the redox potentials of the domain-swapped heterodimer compared to those of the monomers.

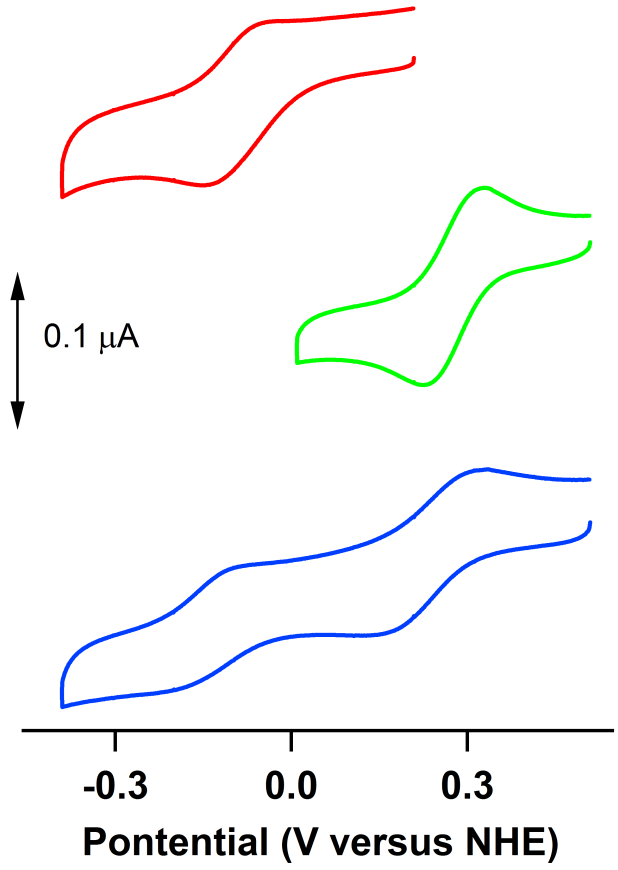

Figure 2.23 Cyclic voltammograms of HT M59A cyt c_{552} monomer (red), PA wild-type cyt c_{551} monomer (green) and the heterodimer of HT*c*-PA*c* and PA*c*-HT*c* M61A (blue). Scan rate, 20 mV/s; buffer, 50 mM potassium phosphate buffer (pH 7.0), containing 200 mM NaCl.

2-2-4 Conclusion

A heterodimer has been constructed by exchanging the N-terminal region containing the heme between chimeric proteins of PA cyt c_{551} and HT M59A cyt c_{552}. The heterodimer contained two different active sites; His–Fe–Met and His–Fe–H_2O. The active sites of the heterodimer maintained the active site structures of PA wild-type cyt c_{551} and HT M59A cyt c_{552}. These results show that domain exchanging concept based on domain-swapping can be utilized to design multi-heme proteins with different active sites.

2-3 References

1. Nagao, S., Osuka, H., Yamada, T., Uni, T., Shomura, Y., Imai, K., Higuchi, Y., Hirota, S. (2012) Structural and oxygen binding properties of dimeric horse myoglobin, *Dalton Trans. 41*, 11378–11385.

2. Lin, Y. W., Nagao, S., Zhang, M., Shomura, Y., Higuchi, Y., Hirota, S. (2015) Rational design of heterodimeric protein using domain swapping for myoglobin, *Angew. Chem. Int. Ed. 54*, 511–515.

3. Berry, E. A., Trumpower, B. L. (1987) Simultaneous determination of hemes *a, b*, and *c* from pyridine hemochrome spectra, *Anal. Biochem. 161*, 1–15.

4. Hayashi, Y., Nagao, S., Osuka, H., Komori, H., Higuchi, Y., Hirota, S. (2012) Domain swapping of the heme and N-terminal α–helix in *Hydrogenobacter thermophilus* cytochrome c_{552} dimer, *Biochemistry 51*, 8608–8616.

5. Battistuzzi, G., Borsari, M., Sola, M., Francia, F. (1997) Redox thermodynamics of the native and alkaline forms of eukaryotic and bacterial class I cytochromes *c*, *Biochemistry 36*, 16247–16258.

6. Oteinowski, Z., Minor, W. (1997) Processing of X-ray diffraction data collected in oscillation mode, *Methods Enzymol. 276*, 307–326.

7. Winn, M. D., Ballard, C. C., Cowtan, K. D., Dodson, E. J., Emsley, P., Evans, P.

R., Keegan, R. M., Krissinel, E. B., Leslie, A. G. W., McCoy, A., Mcnicholas, S. J., Murshudov, G. N., Pannu, N. S., Potterton, E. A., Powell, H. R., Read, R. J., Vagin, A., Wilson, K. S. (2011) Overview of the CCP4 suite and current developments, *Acta Crystallogr. D 67*, 235–242.

8. Brünger, A. T., Adams, P. D., Clore, G. M., DeLano, W. L., Gros, P., Grosse, R. W., Jiang, J. S., Kuszewski, J., Nilges, M., Pannu, N. S., Read, R. J., Rice, L. M., Simonson, T., Warren, G. L. (1998) Crystallography & NMR system: a new software suite for macromolecular structure determination, *Acta Crystallogr. D 54*, 905–921.

9. Emsley, P., Cowtan, K. (2004) Coot: model-building tools for molecular graphics, *Acta Crystallogr. D 60*, 2126–2132.

10. Oikawa, K., Nakamura, S., Sonoyama, T., Ohshima, A., Kobayashi, Y., Takayama, S. J., Yamamoto, Y., Uchiyama, S., Hasegawa, J., Sambongi, Y. (2005) Five amino acid residues responsible for the high stability of *Hydrogenobacter thermophilus* cytochrome c_{552}: reciprocal mutation analysis, *J. Biol. Chem. 280*, 5527–5532.

11. Michel, L. V., Ye, T., Bowman, S. E., Levin, B. D., Hahn, M. A., Russell, B. S., Elliott, S. J., Bren, K. L. (2007) Heme attachment motif mobility tunes

cytochrome *c* redox potential, *Biochemistry 46*, 11753–11760.

12. Levin, B. D., Can, M., Bowman, S. J., Bren, K. L., Elliott, S. J. (2011) Methionine ligand lability in bacterial monoheme cytochromes *c*: an electrochemical study, *J. Phys. Chem. B 115*, 11718–11726.

13. Nagao, S., Ueda, M., Osuka, H., Komori, H., Kamikubo, H., Kataoka, M., Higuchi, Y., Hirota, S. (2015) Domain-swapped dimer of *Pseudomonas aeruginosa* cytochrome c_{551}: structural insights into domain swapping of cytochrome *c* family proteins, *PLoS ONE 10*, e0123653.

Chapter 3

Resonance Raman studies on the oxygenated complexes of Met-depleted *c*-type cytochromes

3-1 Introduction

Besides electron transfer in the respiratory chain of mitochondria, cyt *c* also plays an important role in apoptosis. Hydrophobic interactions between the hydrophobic cavity of cyt *c* and phospholipids induce dissociation of Met80 from the heme iron (Figure 3.1). Met80 of cyt *c* oxidizes the negatively charge phospholipids, which is related to the initial step of apoptosis (*1, 2*). As a result, the peroxidase activity of cyt *c* increases.

The axial ligands play important roles in modulation of the structure and function of heme proteins, such as redox potential, electronic structure, spin state and electron transfer rate (*3-8*). Redox potential of cyt *c* was decreased from +260 mV to -170 mV in the presence of cardiolipin, because Met dissociated from the heme iron (*9*). Cyt *c* may react with external ligands by removal of the heme-coordinating Met. The oxygenated species of yeast iso-1 M80A cyt *c* mutant has been reported by Bren and Gray (Figure 3.2) (*10*). But the details of the active site character are as yet unrevealed. In this study, resonance Raman studies were performed to reveal the detailed character of the oxygenated species of heme coordinating Met-depleted *c* type cytochromes.

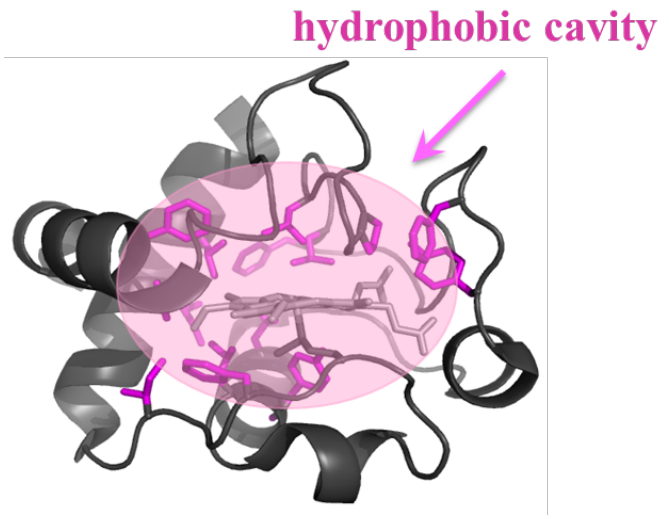

Figure 3.1 Structure of horse cyt *c* (PDB ID code: 1HRC). The heme is shown as a gray stick model. Hydrophobic side-chain atoms are shown as pink stick models.

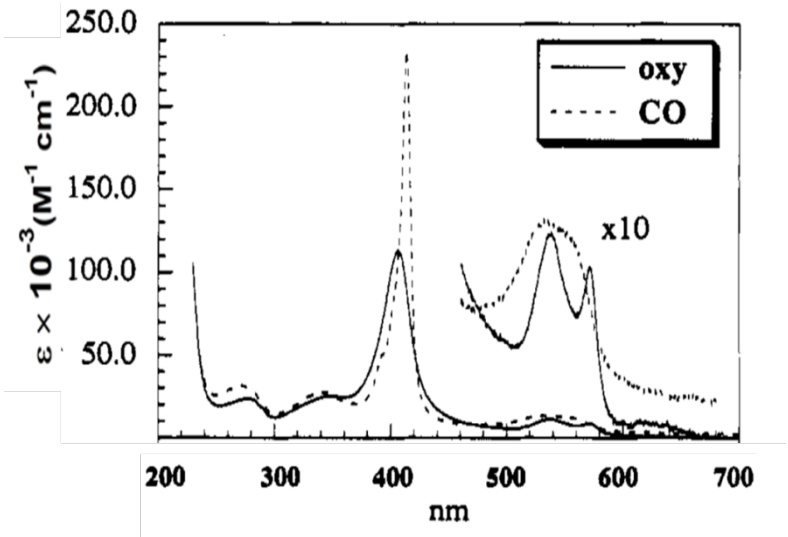

Figure 3.2 Absorption spectra of oxygenated and carbon monoxide bound species of yeast iso-1 M80A cyt *c* (*10*).

3-2 Materials and methods

3-2-1 Plasmid for horse M80A cyt *c*

Plasmid for expression of horse cyt *c* was constructed as described previously (*11*). Met80 of horse cyt *c* was substituted with Ala (horse M80A cyt *c*). Point mutation of Met to Ala was introduced by PCR-based *in vitro* mutagenesis using forward and reverse primers (Eurofins genomics) (Table 3.1), and Primer STAR max DNA polymerase (Takara Bio). Plasmid DNA were prepared using *E. coli* DH5α cells, and purified with the QIAprep spin Mini prep kit (Qiagen). DNA sequencing was conducted with the BigDye Terminator version 3.1 cycle sequencing kit (Applied Biosystems, Inc., Foster City, CA) and an ABI PRISM 3100 genetic analyzer sequencing system (Applied Biosystems, Inc.). The constructed plasmids were introduced into *E. coli* Rosetta^{TM} 2(DE3)pLysS cells.

3-2-2 Purification of cyt *c* mutants

Horse M80A cyt *c* was overproduced in *E. coli* cells. The *E. coli* cells were grown aerobically in 25 g/L LB broth at 37 ºC until the OD_{600} reached around 1.5-1.8, and then harvested by centrifugation (8,000 g, 5 min, 4 ºC). After centrifugation, the cells were suspended in a minimal volume of 50 mM potassium phosphate buffer (pH

7.0), and subsequently the cells were freezed in liquid nitrogen and melted in flowed water at least 3 times. DNase was added to the protein solution and stirred for 1 hour at 4 ºC. The supernatant was collected after centrifugation (13,700 g, 30 min, 4 ºC). The protein solution was dialyzed overnight at 4 ºC with 5 mM potassium phosphate buffer, pH 7.0. The proteins were oxidized by an addition of excess (~10 fold) potassium ferricyanide. The protein solution was purified by cation exchange chromatography (CM-cellulose column (Wako), HiTrap SP column (GE healthcare)), and size exclusion chromatography (HiLoad 26/60 Superdex 75, GE healthcare) using the FPLC system (BioLogic DuoFlow 10, Bio-Rad, CA) at 4 ºC with 50 mM potassium phosphate buffer, pH 7.0. HT M59A cyt c_{552} mutant was purified as described above in chapter 2.

The molar extinction coefficient of horse M80A cyt *c* has been reported (*11, 12*). The molar extinction coefficient of HT M59A cyt c_{552} (ε = 160,000 ± 2000 $M^{-1}cm^{-1}$ at 401 nm) as described above in chapter 2. The concentrations of the proteins were calculated from the absorbance at 406 nm and 401 nm with the absorption coefficient for horse M80A cyt *c* and HT M59A cyt c_{552}, respectively.

3-2-3 Optical absorption measurement

Optical absorption spectra were measured with a UV-2450 spectrophotometer

(Shimadzu, Japan) using a 1-cm-path-length quartz cell at 25 °C. The oxidized horse M80A cyt *c* species was placed under N_2 atmosphere using a vacuum line and reduced by an addition of excess (~5 fold) dithionite to the protein solution. The dithionite solution (50 mM, ~1.5 μL) was added to the oxidized horse M80A cyt *c* solution (~10 μM, 1.5 mL). The HT M59A cyt c_{552} was treated in the same procedures as those of horse M80A cyt *c*. The reduced and oxygenated species of horse M80A cyt *c* and HT M59A cyt c_{552} were confirmed by their absorption spectra.

For autoxidation reaction experiments, reduced horse M80A cyt *c* (~1 mM) and HT M59A cyt c_{552} (~0.5 mM) were diluted (~100 times) with 0.7 mL of 50 mM potassium phosphate buffer, pH 7.0 (in air) to obtain the oxygenated species. The final concentration of horse M80A cyt *c* was ~10 μM, and the final concentration of HT M59A cyt c_{552} was ~5 μM. The time dependent UV-vis spectra were measured.

3-2-4 Resonance Raman measurements

Resonance Raman scattering of horse M80A cyt *c* and HT M59A cyt c_{552} was excited at 405.1 nm with a diode laser (ONDAX SureLook^{TM}, Model LM-403-PLR-40-2) at room temperature and detected with a liquid nitrogen-cooled CCD (Roper Scientific, 7375-0001) attached to a single polychromator (SPEX, 750M).

A spinning cell was used to avoid the damage of the sample. The slit width was set to 110 μm. The laser power was adjusted to 3.5-3.8 mW at the sample point. The sample cell was spun at 2000 rpm to avoid laser heating. Concentrated oxidized horse M80A cyt *c* (1 mM) solution was placed under N_2 atmosphere using a vacuum line, and reduced by an addition of dithionite (final concentration ~5 mM) to the protein solution. To obtain $^{16}O_2$ adducts of horse M80A cyt *c*, reduced horse M80A cyt *c* solution was diluted 40 times with $^{16}O_2$-saturated buffer. The $^{18}O_2$ complexes of horse M80A cyt *c* was obtained with same method using $^{18}O_2$ instead of $^{16}O_2$. The $^{16}O_2$ and $^{18}O_2$ adducts of HT M59A cyt c_{552} were obtained as same method with those of horse M80A cyt *c*. The final concentrations of horse M80A cyt *c* and HT M59A cyt c_{552} were adjusted to 20 μM and 10 μM, respectively. Raman shifts were calibrated with indene and CCl_4 as standards. Accuracy of the peak positions of the resonance Raman bands was ± 1 cm^{-1}.

Table 3.1 Nucleotide sequences of primers.

Primer	Sequence[a]
Horse cyt *c*-M80A-fw	ACAAAAGCGATCTTTGCTGGCATTAAG
Horse cyt *c*-M80A-rv	AAAGATCGCTTTTGTTCCAGGGATGTA

[a]Underlines indicate the nucleotides for the modified amino acid.

3-3 Results and discussion

The Soret band of oxidized horse M80A cyt *c* was observed at 406 nm and its Q bands were observed at 533 nm and 560 nm, which were very similar to reported results (Figure 3.3, black) (*10, 12*). For reduced M80A cyt *c*, the Soret band and Q-bands were observed at 412 nm and 550 nm, respectively (Figure 3.3, blue). The reduced M80A cyt *c* reacted with oxygen, and the Soret band shifted to 408 nm and the Q-bands were observed at 538 nm and 571 nm (Figure 3.3, red). Autoxidation reaction occurred, but the rate was slow (Figure 3.4). These results indicate that oxygenated horse M80A cyt *c* is stable.

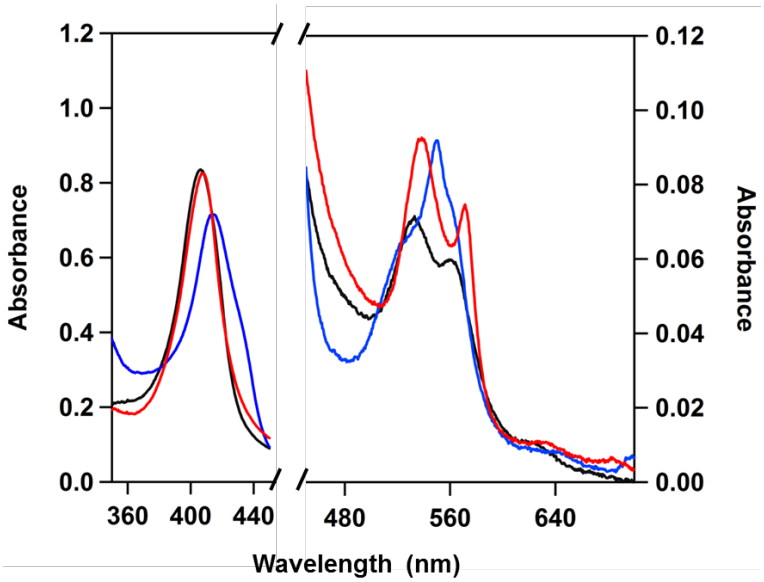

Figure 3.3 Optical absorption spectra of horse M80A cyt *c*: Black, oxidized species; blue, reduced species; red, oxygenated species. Measurement conditions: sample concentration (heme), ~10 μM; solvent, 50 mM potassium phosphate buffer (pH 7.0); temperature, 25 °C.

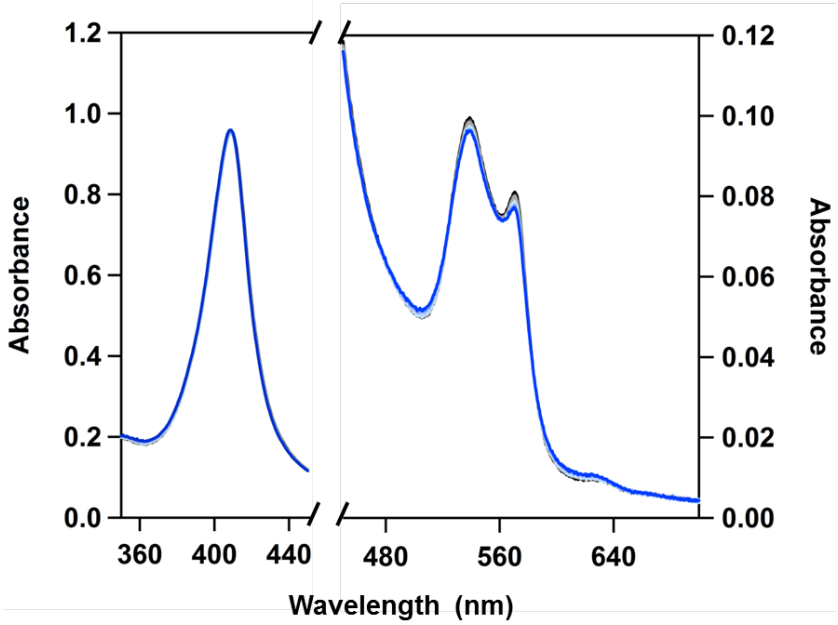

Figure 3.4 Time dependent UV-vis spectra of oxygenated horse M80A cyt *c*. The oxygenated species was obtained by dilution of reduced horse M80A cyt *c* with buffer. The spectra were recorded after 15 seconds (black), 5 min, 10 min, 20 min, 30 min, 60 min, 90 min, and 120 min (blue). Measurement conditions: sample concentration (heme), ~10 μM; solvent, 50 mM potassium phosphate buffer (pH 7.0); temperature, 25 °C.

The resonance Raman measurements were performed to reveal the detail character of oxygenated horse M80A cyt *c* (Figure 3.5). In the high frequency region, the strongest band (ν_4 band) is known as an oxidation state marker band (*13-18*). In the spectrum of the oxidized species, the ν_4 band was observed at 1376 cm^{-1} (Figure 3.5a). On the other hand, the ν_4 band was observed at 1357 cm^{-1} in the spectrum of the reduced species (Figure 3.5b). These frequencies were in good agreement for the ferric and ferrous states of traditional heme proteins. In the spectrum of the oxygenated

species, the ν_4 band was observed at 1377 cm^{-1}, due to decrease in the electron density of the heme iron by coordination of the oxygen molecule (Figure 3.5c). The ν_3 band is sensitive to the oxidation and spin states (*14*, *20*). In the spectrum of the oxidized species, the ν_3 band was observed at 1503 cm^{-1}, typical for a low-spin ferric species (Figure 3.5a). This frequency indicates that the OH^- is coordinated to the heme iron in the oxidized state. In the spectrum of the reduced species, the ν_3 band was observed at 1469 cm^{-1}, indicating a high-spin 5-coordinated species (Figure 3.5b).

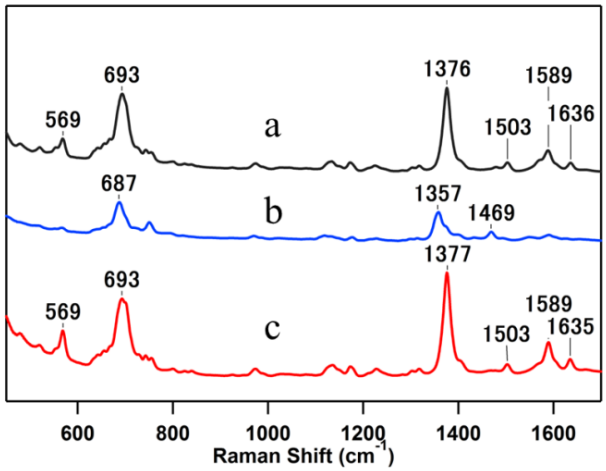

Figure 3.5 Resonance Raman spectra of (a) oxidized, (b) reduced, and (c) oxygenated of horse M80A cyt *c*. Measurement conditions: sample concentration (heme), 20 μM; solvent, 50 mM potassium phosphate buffer (pH 7.0); laser power, 3.5 mW; excitation, 405.1 nm; accumulation, (a, b) 5 min and (c) 20 min. temperature, room temperature.

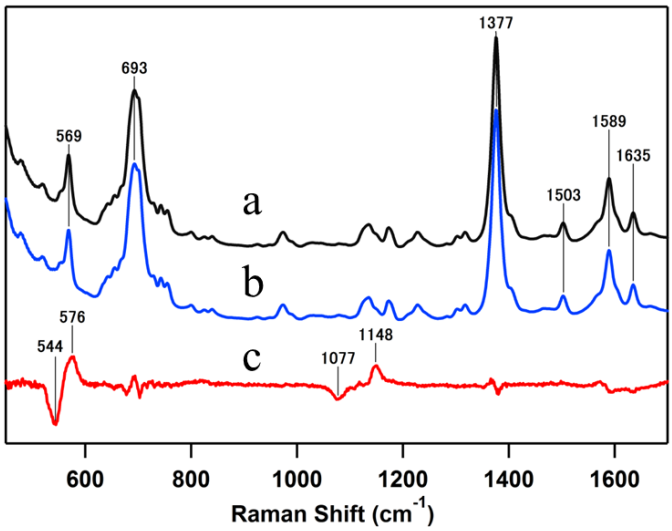

Figure 3.6 Resonance Raman spectra of oxygenated horse M80A cyt *c*. (a) $^{16}O_2$ adduct (black); (b) $^{18}O_2$ adduct (blue); (c) the difference spectrum between the spectra of the $^{16}O_2$ adduct and $^{18}O_2$ adduct and is expanded 20 times. Measurement conditions: sample concentration (heme), 20 μM; solvent, 50 mM potassium phosphate buffer (pH 7.0); temperature, room temperature; laser power, 3.5 mW; excitation, 405.1 nm; accumulation, 20 min.

In the difference spectrum between the spectra of the $^{16}O_2$ adduct and the $^{18}O_2$ adduct, two difference patterns were observed with all other major Raman bands cancelled out between the spectra of $^{16}O_2$ and $^{18}O_2$ adducts (Figure 3.6c). A peak at 576 cm^{-1} in the spectrum of the $^{16}O_2$ species shifted to 544 cm^{-1} in the spectrum of the $^{18}O_2$ species. A peak at 1148 cm^{-1} in the spectrum of the $^{16}O_2$ species shifted to 1077 cm^{-1} in the spectrum of the $^{18}O_2$ species. From the frequencies and isotope frequency shifts, the 576 cm^{-1} band is assigned to the Fe–O stretching mode, and the 1148cm^{-1} band is assigned to the O–O stretching mode. However, the enhancement of the $\nu_{O\text{-}O}$ band was

rather special for His-ligated hemeproteins. Enhancement of the ν_{Fe-O} mode has been suggested to occur when a H-bonding network exists between the heme-bound oxygen and its surrounding environment. In the structure of yeast iso-1 K72A cyt *c*, water molecules existed around the heme open cavity due to the dissociation of Met80 from the heme iron (Figure 3.7a). A hydrogen-bond formed between Tyr67 and the oxygen atom of H_2O or OH^-, and a hydrogen-bonding network existed around the heme. Moreover, in the domain-swapped dimeric structure of horse cyt *c*, Met was also dissociated from the heme iron, and a H-bond existed between the heme-bound oxygen of H_2O/OH^- and Tyr67 (Figure 3.7b). Therefore, the enhancement of the ν_{O-O} mode in cyt c may be due to the H-bonding network around the heme.

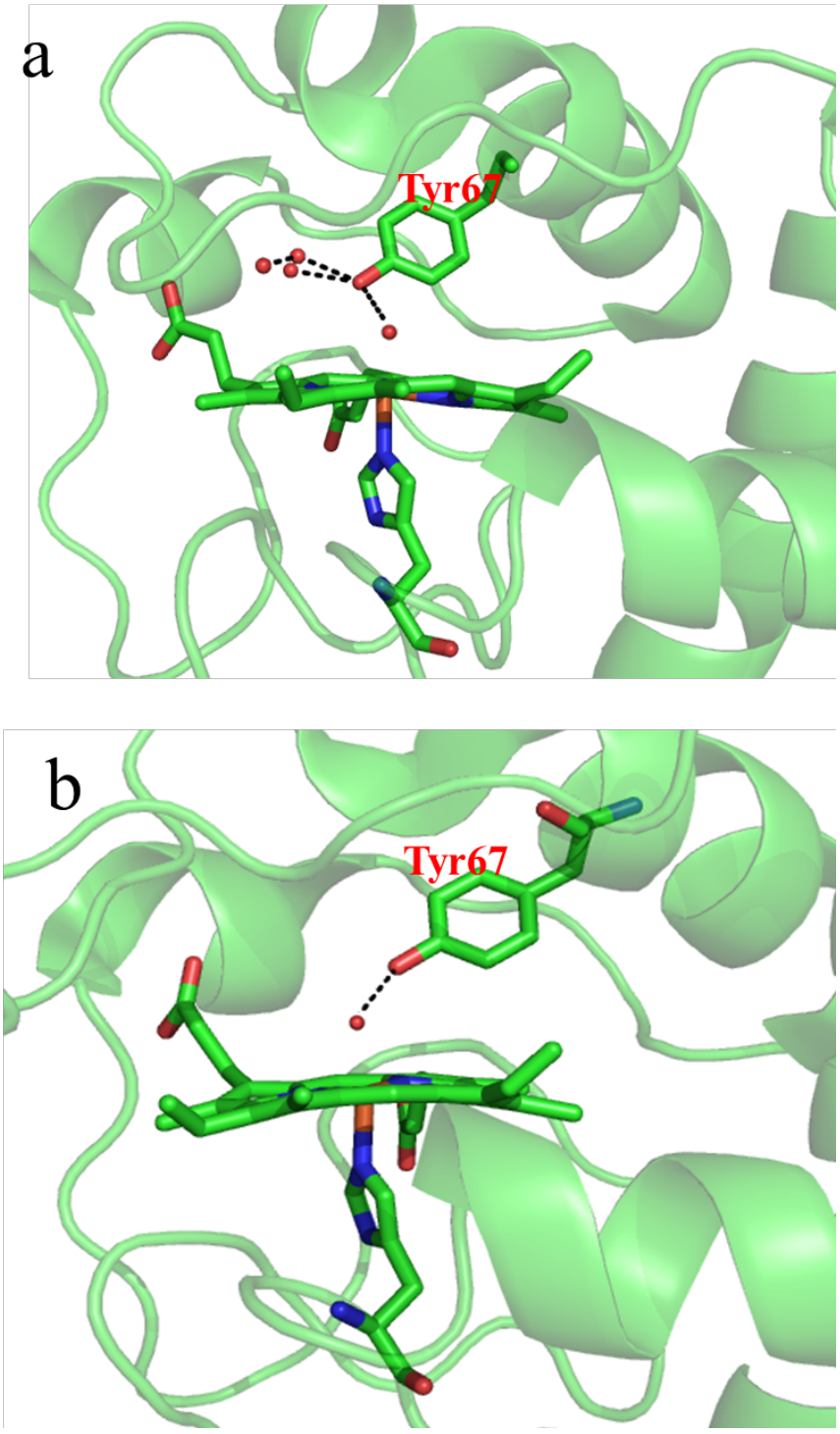

Figure 3.7 H-bond network around the heme of (a) yeast iso-1 K72A cyt *c* (PDB ID code: 4MU8) and (b) dimeric horse cyt *c* (PDB ID code: 3NBS). The heme and Tyr67 and His18 are shown as stick models. Water molecules at the heme pocket are shown as red spheres.

To check the Fe-O stretching mode for other *c*-type cyt *c*, I prepared the oxygenated species of heme-coordinating methionine depleted HT M59A cyt c_{552}. The oxidized, reduced, and oxygenated species of HT M59A cyt c_{552} were prepared with same method as those of horse M80A cyt *c*.

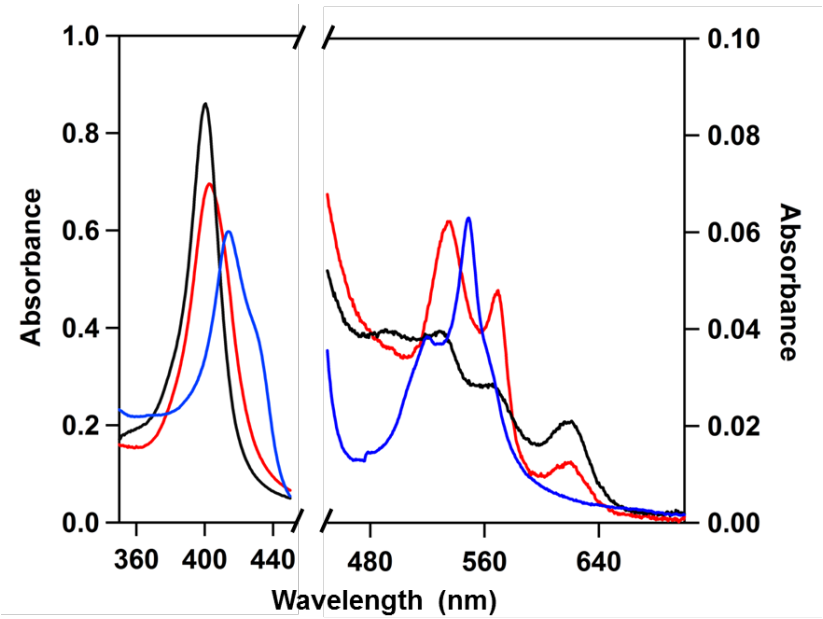

Figure 3.8 Optical absorption spectra of HT M59A cyt c_{552}. Black, oxidized species; blue, reduced species; red, oxygenated species. Measurement conditions: sample concentration (heme), ~6 μM; solvent, 50 mM potassium phosphate buffer (pH 7.0); temperature, 25°C.

The absorption spectra of oxidized, reduced, and oxygenated species of HT M59A cyt c_{552} are shown in Figure 3.8. The Soret band of oxidized HT M59A cyt c_{552} was observed at 400 nm and its Q bands were observed at 529 nm, 560 nm, and 620 nm (Figure 3.8, black). For reduced HT M59A cyt c_{552}, the Soret band was observed at 415

nm, and the Q-band shifted to 549 nm (Figure 3.8, blue). Reduced HT M59A cyt c_{552} reacted with an oxygen molecule, and the Soret band shifted to 403 nm and the Q-bands were observed at 520 nm and 550 nm (Figure 3.8, red). These results indicate formation of the oxygenated species of HT M59A cyt c_{552}. Autoxidation of the oxygenated species of HT M59A cyt c_{552} also occurred (Figure 3.9).

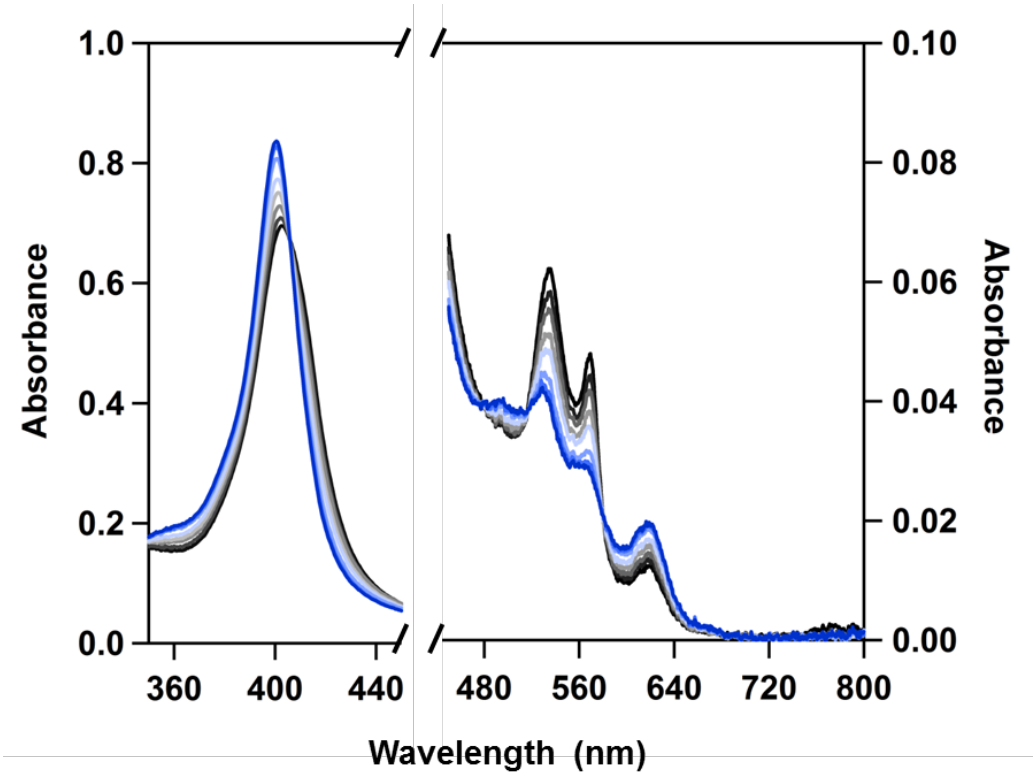

Figure 3.9 Time dependent UV-vis spectra of oxygenated HT M59A cyt c_{552}. The oxygenated species was obtained by dilution of reduced HT M59A cyt c_{552} with buffer. The spectra were recorded after 15 seconds (black), 5 min, 10 min, 20 min, 30 min, 60 min, 90 min, and 120 min (blue). Measurement conditions: sample concentration (heme), ~6 μM; solvent, 50 mM potassium phosphate buffer (pH 7.0); temperature, 25 °C.

Resonance Raman measurements were also performed to investigate the oxygenated HT M59A cyt c_{552} species (Figure 3.10). The black and blue spectra in Figure 3.10 represent the $^{16}O_2$ adduct and $^{18}O_2$ adduct of HT M59A cyt c_{552}, respectively. The red spectrum represents the difference spectrum between the spectra of the $^{16}O_2$ adduct and $^{18}O_2$ adduct and is expanded 20 times (Figure 3.10c). In the difference spectrum, the different patterns were observed with all other major Raman bands cancelled out between the spectra of $^{16}O_2$ and $^{18}O_2$ adducts. A peak at 580 cm^{-1} in the spectrum of the $^{16}O_2$ species shifted to 553 cm^{-1} in the spectrum of the $^{18}O_2$ species. This band is assigned to the Fe-O stretching mode.

The ν_{Fe-O} frequencies of horse M80A cyt *c* and HT M59A cyt c_{552} were higher compared to those of other oxygenated hemeproteins, such as Mb and Hb (Table 3.2) (*20-22*). The Fe-O stretching frequencies have been shown to decrease when the electron density of the heme decreases. In cyt *c,* the ligand coordinated to the heme iron may be relatively strong compared to those of other heme proteins. The strong Fe-O bond character of *c*-type cyts may be related to the high stabilities of their oxygenated species as well as the peroxidase activity of cyt *c*.

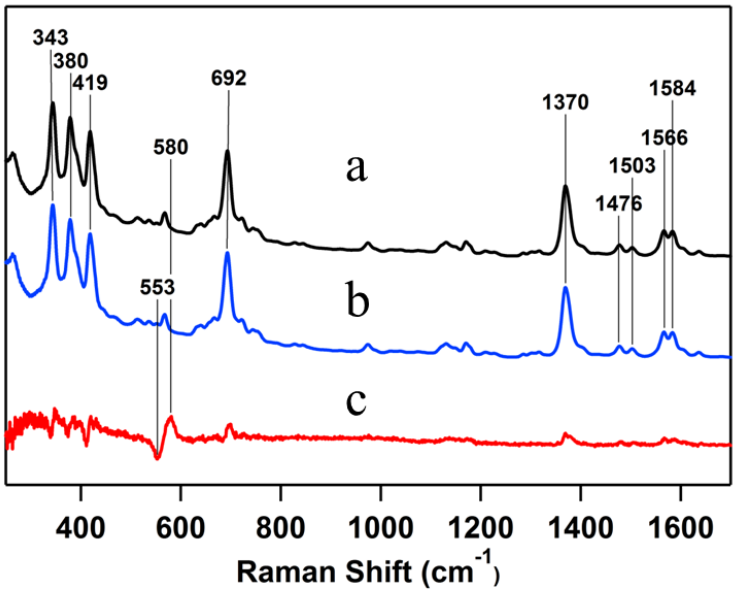

Figure 3.10 Resonance Raman spectra of oxygenated HT M59A cyt c_{552}. (a) $^{16}O_2$ adduct (black); (b) $^{18}O_2$ adduct (blue); (c) the difference spectrum between the spectra of the $^{16}O_2$ adduct and $^{18}O_2$ adduct and is expanded 20 times. Measurement conditions: sample concentration (heme), 10 μM; solvent, 50 mM potassium phosphate buffer (pH 7.0); temperature, room temperature; laser power, 3.8 mW; excitation, 405.1 nm; accumulation, 20 min.

Table 3.2 The Fe-O stretching frequencies of hemeproteins.

Hemeproteins	$\nu_{Fe\text{-}O}$ (cm^{-1})
Hemoglobin	569
Myoglobin	571
Horseradish peroxidase	562
Cytochrome *c* oxidase	571
Horse M80A cyt *c*	576
HT M59A cyt c_{552}	580

3-4 Conclusions

The replacement of Met to Ala in cytochromes created a binding site for an oxygen molecule. The $\nu_{Fe\text{-}O}$ and $\nu_{O\text{-}O}$ modes of horse M80A cyt *c* and the $\nu_{Fe\text{-}O}$ mode of HT M59A cyt c_{552} were observed. Interestingly, the $\nu_{Fe\text{-}O}$ frequencies of Met-depleted of *c*-type cyts were relatively high compared to those of other heme proteins. The strong Fe-O bond character may be related to the high stability of the oxygenated species of *c*-type cytochrome, as well as the peroxidase activity of cyt *c*.

3-5 References

1. Kagan, V. E., Borisenko, G. G., Tyurina, Y. Y., Tyurin, V. A., Jiang, J., Potapovich, A. I., Kini, V., Amoscato, A. A., Fujii, Y. (2004) Oxidative lipidomics of apoptosis: redox catalytic interactions of cytochrome *c* with cardiolipin and phosphatidylserine, *Free Radical Biol. Med. 37*, 1963–1985.

2. Kagan, V. E., Yalowich, J. C., Borisenko, G. G., Tyurina, Y. Y., Tyurin, V. A., Thampatty, P., Fabisiak, J. P. (1999) Mechanism-based chemopreventive strategies against etoposide-induced acute myeloid leukemia: free radical/antioxidant approach, *Mol. Pharmacol. 56*, 494–506.

3. Adrienne, L. R., Gray, H. B. (1991) Semisynthesis of axial-ligand (position 80) mutants of cytochrome *c*, *J. Am. Chem. Soc. 113*, 1038–1040.

4. Bren, K. L., Gray, H. B. (1993) Ligand binding to Ala80 cytochrome *c*, *J. Inorg. Biochem. 51*, 10382–10383.

5. Bushnell, G. W., Louie, G. V., Brayer, G. D. (1990) High-resolution three-dimensional structure of horse heart cytochrome *c*, *J. Mol. Biol. 214*, 585–595.

6. Dickerson, R. E., Takano, T., Eisenberg, D., Kallai, O. B., Samson, L., Cooper, A., Margoliash, E. (1971) Ferricytochrome *c*: general featrues of the horse and

bonito protein at 2.8 Å resolution, *J. Biol. Chem. 246*, 1511–1535.

7. Wallace, C. J., Lewis, C. I. (1992) Functional role of heme ligation in cytochrome *c*, *J. Biol. Chem. 267*, 3852–3861.

8. Senn, H., Wüthrich, Kurt. (1985) Amino acid sequence, heme-iron coordination geometry and functional properties of mitochondrial and bacterial *c*-type cytochromes, *Q. Rev. Biophys. 18*, 111–134.

9. Basova, L. V., Kurnikov, I. V., Wang, L., Ritov, V. B., Belikova, N, A., Vlasova, I. I., Pacheco, A. A., Winnica, D. E., Peterson, J., Bayir, H.l., Waldeck, D. H., Kagan, V. E. (2007) Cardiolipin switch in mitochondria: shutting off the reduction of cytochrome *c* and turning on the peroxidase activity, *Biochemistry 46*, 3423–3434

10. Bren, K. L., Gray, H. B. (1993) Structurally engineered cytochromes with novel ligand-binding sites: oxy and carbon monoxy derivatives of semisynthetic horse heart Ala80 cytochrome *c*, *J. Am. Chem. Soc. 115*, 10382–10383.

11. Kobayashi, H., Nagao, S., Hirota, S. (2016), Charecterization of the cytochrome *c* membrance-binding site using cardiolipin-containing bicells with NMR, *Angew. Chem. Int. Ed. 55*, 14019–14022.

12. Lu, Y., Casimiro, D. R., Bren, K. L., Richards, J. H., Gray, H. B. (1993)

Structurally engineered cytochromes with unusual ligand-binding properties: expression of *Saccharomyces cerevisiae* Met80Ala iso-1-cytochrome *c*, *Proc. Natl. Acad. Sci. U. S. A. 90*, 11456–11459.

13. Kitagawa, T., Kyogoku, Y., Iizuka, T., Saito, M. I. (1976) Nature of the iron-ligand bond in ferrous low spin hemoproteins studied by resonance Raman scattering, *J. Am. Chem. Soc. 98*, 5169–5173.

14. Rimai, L., Salmeen, I., Petering, D. H. (1975) Comparison of the resonance Raman spectra of carbon monoxy and oxy hemoglobin and myoglobin. similarities and differences in heme electron distribution, *Biochemistry 14*, 378–382.

15. Spiro, T. G., Burke, J. M. (1976) Protein control of porphyrin conformation. comparison of resonance Raman spectra of heme proteins with mesoporphyrin IX analogs, *J. Am. Chem. Soc. 98*, 5482–5489.

16. Yamamoto, T., Palmer, G., Gill, D., Salmeen, I. T., Rimai, L. (1973) The valence and spin state of iron in oxyhemoglobin as inferred from resonance Raman spectroscopy, *J. Biol. Chem. 248*, 5211–5213.

17. Vogel, K. M., Kozlowski, P. M., Zgierski, M. Z., Spiro, T. G. (1999) Determinants of the FeXO (X = C, N, O) vibrational frequencies in heme

adducts from experiment and density functional theory, *J. Am. Chem. Soc. 121*, 9915–9921.

18. Hu, S., Morris, I. K., Singh, J. P., Smith, K. M., Spiro, T. G. (1993) Complete assignment of cytochrome *c* resonance Raman spectra *via* enzymic reconstitution with isotopically labeled hemes, *J. Am. Chem. Soc. 115*, 12446–12458.

19. Schweitzer, S. R., Bobinger, U., Dreybrodt, W. (1991) Multimode analysis of depolarization ratio dispersion and excitation profiles of seven Raman fundamentals from the heme group in ferrocytochrome *c*, *J. Raman Spectrosc. 22*, 65–78.

20. Hirota, S., Li, T., Phillips, G. N., Olson, J. S., Mukai, M., Kitagawa, T. (1996) Perturbation of the Fe−O_2 bond by nearby residues in heme pocket: observation of $\nu_{Fe\text{-}O}$ Raman bands for oxymyoglobin mutants, *J. Am. Chem. Soc. 118*, 7845–7846.

21. Kerr, E. A., Yu, N. T., Bartnicki, D. E., Mizukami, H. (1985) Resonance Raman studies of CO and O_2 binding to elephant myoglobin, *J. Biol. Chem. 260*, 8360–8365.

22. Nagai, K., Kitagawa, T., Morimoto, H. (1980) Quaternary structures and low frequency molecular vibrations of haems of deoxy and oxyhaemoglobin studied by resonance Raman scattering, *J. Mol. Biol. 136*, 271–289.

Chapter 4

Conclusion

Two heterodimers of *c*-type cytochromes with different active sites have been successfully constructed based on domain-swapping. The swapped domains contained the N-terminal region and heme. The heterodimers contained two different active sites, His–Fe–Met and His–Fe–H_2O. Each active site of HT wild-type–M59A cyt c_{552} heterodimer exhibited an electron density of an average of His–Fe–Met and His–Fe–H_2O coordination. The active sites of the HT*c*-PA*c* and PA*c*-HT*c* M61A heterodimer maintained the active site structures of PA wild-type cyt c_{551} and HT M59A cyt c_{552}. These results show that artificial heme protein oligomers with different active sites and ligand binding properties can be constructed based on domain swapping.

The ν_{Fe-O} and ν_{O-O} modes of horse M80A cyt *c* and the ν_{Fe-O} mode of HT M59A cyt c_{552} were observed. Interestingly, the ν_{Fe-O} frequencies of Met-depleted of *c*-type cyts were relatively high compared any other ν_{Fe-O} frequency detected for oxygenated heme proteins so far. The strong Fe−O bond character of *c*-type cyts may be related to the high stabilities of their oxygenated species, as well as the peroxidase activity of cyt *c*.

For future studies, properties of the oligomers may be applied to protein engineering and medical application such as sensors and enzymes. Other multi-heme proteins with different active sites and ligand binding properties may be constructed

by using domain-swapping concept with new functions.

ACKNOWLEDMENTS

I would like to express my deepest gratitude to my academic supervisor, Professor Shun Hirota, for his patience, instructive guidance and constant encouragement. He offered me valuable suggestion in all the time of research. I have learned a great deal during the periods of my study in Japan.

Second, I would like to express my sincere thanks to my supervisor committee, Professor Hiroko Yamada, Associate Professor Tsuyoshi Ando and Assistant Professor Masaru Yamanaka for their valuable suggestions and comments. Especially Assistant Professor Masaru Yamanaka, he gives me big help to teach biological knowledge.

I would like to say thanks to the president of Nara Institute Science and Technology and the Dean of the Graduate School of Materials Science for supporting my research and daily life. I am also very grateful to the staffs of International Student Affair Section for helping my daily life.

Special thanks should go to express my heartfelt gratitude to Assistant Professor Takashi Matsuo, Assistant Professor Satoshi Nagao and Hulin Tai for their help about experiments. I also appreciate and thank to Kaoru Teshima and Masako Tashiro for their kindness help in the daily life.

I would like to thank Yugo Hayashi, Hisashi Kobayashi, Akiya Oda, Robby

Noor Cahyono, Hongxu Yang and other members of Supramolecular Science Laboratory, for their support in experiment and friendship.

Finally, I am grateful to my parents for their support, they always encourage me to try my best. My brother always supports to complete these works.

LIST OF PUBLICATION

Rational design of domain swapping-based c-type cytochrome heterodimers using chimeric proteins

Mohan Zhang, Tsukasa Nakanishi, Masaru Yamanaka, Satoshi Nagao, Sachiko Yanagisawa, Yasuhito Shomura, Naoki Shibata, Takashi Ogura, Yoshiki Higuchi, and Shun Hirota

ChemBioChem, **18**(17), 1712-1715 (2017).

Rational design of heterodimeric protein using domain swapping for myoglobin

Ying-Wu Lin, Satoshi Nagao, Mohan Zhang, Yasuhito Shomura, Yoshiki Higuchi, and Shun Hirota

Angewandte Chemie International Edition, **54**(2), 511-515 (2015).